Multiple plates subducting beneath Colombia, as illuminated by seismicity and velocity from the joint inversion of seismic and gravity data

Syracuse, Ellen M.
Maceira, Monica
Prieto, German A.
Zhang, Haijiang
Ammon, Charles J.

To be published in: Earth and Planetary Science Letters

DOI to publisher's version: 10.1016/j.epsl.2016.03.050

Permalink to record: http://permalink.lanl.gov/object/view?what=info:lanl-repo/lareport/LA-UR-15-29234

Multiple plates subducting beneath Colombia, as illuminated by seismicity and velocity from the joint inversion of seismic and gravity data

Ellen M. Syracuse[1]*
Monica Maceira[1]
Germán A. Prieto[2]
Haijiang Zhang[3]
Charles J. Ammon[4]

[1]EES-17, Los Alamos National Laboratory, P.O. Box 1663, MS F665, Los Alamos, NM 87545
[2]Department of Earth, Atmospheric and Planetary Science, Massachusetts Institute of Technology, 77 Massachusetts Avenue, Cambridge, MA 01239
[3]Laboratory of Seismology and Physics of Earth's Interior, School of Earth and Space Sciences, University of Science and Technology of China, 96 Jinzhai Road, Hefei 230026, Anhui, China
[4]Department of Geosciences, Pennsylvania State University, 440 Deike Building, University Park, PA 16802

*Corresponding author: syracuse@lanl.gov

Highlights

- Joint inversion provides a clearer image of subduction than body-wave-only tomography
- Normal-dip subduction of Nazca beneath volcanogenic southern Colombia
- Non-volcanogenic flat-slab subduction of Nazca and Caribbean plates further north
- Slab tear between normally dipping and flat sections of Nazca plate

Abstract

Subduction beneath the northernmost Andes in Colombia is complex. Based on seismicity distributions, multiple segments of slab appear to be subducting, and arc volcanism ceases north of 5° N. Here, we illuminate the subduction system through hypocentral relocations and Vp and Vs models resulting from the joint inversion of local body wave arrivals, surface wave dispersion measurements, and gravity data. The simultaneous use of multiple data types takes advantage of the differing sensitivities of each data type, resulting in velocity models that have improved resolution at both shallower and deeper depths than would result from traditional travel time tomography alone. The relocated earthquake dataset and velocity model clearly indicate a tear in the Nazca slab at 5° N, corresponding to a 250-km shift in slab seismicity and the termination of arc volcanism. North of this tear, the slab is flat, and it comprises slabs of two sources: the Nazca and Caribbean plates. The Bucaramanga nest, a small region of among the most intense intermediate-depth seismicity globally, is associated with the boundary between these two plates and possibly with a zone of melting or elevated water content, based on reduced Vp and increased Vp/Vs. We also use relocated seismicity to identify two new faults in the South American plate, one related to plate convergence and one highlighted by induced seismicity.

Keywords

Flat-slab, Bucaramanga nest, slab tear, body wave, surface wave, gravity

1. Introduction

The Colombian subduction zone is complex, and there are competing hypotheses regarding its structure. Converging or colliding with the western edge of the South American plate are, from north to south, the Caribbean plate, the Panama arc, and the Nazca plate (Figure 1). Wadati-Benioff zone seismicity beneath Colombia is located in two bands, offset by a ~250 km right-lateral shift at 5° N [Pennington, 1981], which coincides with the northern termination of arc volcanism (Figure 2). The slab north of this shift is often referred to as the Bucaramanga segment, and the southern slab is often referred to as the Cauca segment [Pennington et al., 1981]. Within the Bucaramanga segment lies the Bucaramanga nest, a localized region of seismicity containing among the highest concentrations of intermediate-depth seismicity globally [e.g., Prieto et al., 2012].

There are several proposed models of the interactions between these plates and the sources of the Bucaramanga and Cauca segments. One group of models attributes the Cauca segment to a Nazca origin and the Bucaramanga segment to a Caribbean origin, with the Bucaramanga nest located within the Caribbean plate [Schneider et al., 1987; Malavé and Suárez, 1995; Taboada et al., 2000; Cortés and Angelier, 2005; Vargas et al., 2007; Prieto et al., 2012; Yarce et al., 2014]. In several models, the northern edge of the Cauca segment and the southern edge of the Bucaramanga segment overlap [Taboada et al., 2000; Cortés and Angelier, 2005; Vargas et al., 2007]. In some models, the Bucaramanga nest is associated with the tearing off of a deeper portion of the slab [Cortés and Angelier, 2005; Vargas and Mann, 2013]. In other models, the Bucaramanga nest is within the Nazca plate, with an overlapping Caribbean slab to the north [van der Hilst and Mann, 1994] or at the boundary between the Nazca and Caribbean slabs

[Corredor, 2003; Zarifi et al., 2007; Sanchez-Rojas and Palma, 2014]. Others focus on the origin of the ~250 km offset in slab seismicity, some attributing it to a tear in the Nazca slab [Chiarabba et al., 2015], with a transition to Caribbean slab at an undefined location further north [Vargas and Mann, 2013] or at the Bucaramanga nest [Zarifi et al., 2007].

We provide insight to the structure of this subduction system by jointly inverting body wave, surface wave, and gravity data for Vp, Vs, and earthquake hypocenters in Colombia. We make use of the recent improvement in the RSNC (Red Sísmica Nacional de Colombia) instrumentation to provide some of the highest-resolution seismic velocity images of Colombia to date.

2. Data

2.1 Body waves

Continuous seismic waveforms, catalog locations, and P- and S-arrivals for 2010 through 2014 are provided by the RSNC (Figures 1, 2), with additional data from two nearby Global Seismograph Network stations, OTAV and SDV, totaling data from 84 stations. When possible, additional arrival picks are made on the raw waveforms to supplement the local catalog. Erroneous catalog arrivals are identified by eye and adjusted or deleted as appropriate.

Due to the high density of earthquakes in the Bucaramanga nest [e.g., Prieto et al., 2012], which comprised almost half of the RSNC catalog within the study region, only the best-recorded 10% of earthquakes within the nest are included in the joint tomographic and relocation inversion; this helps normalize the ray sampling within the region. For earthquakes elsewhere in the study area, only those with five or more P arrivals are included. This yields a dataset of 1340 earthquakes, 24400 P arrivals, and 16600 S arrivals (Figures 2, 3). In addition to the absolute P- and S-arrival times, differential catalog and cross-correlated arrival times are calculated [Waldhauser and Ellsworth, 2000; Du et al., 2004] and included in the inversion to further improve the relative hypocentral relocations.

2.2 Surface waves

Surface waves are included in the joint inversion in the form of a dispersion curve at each horizontal grid node within the study area. These curves are sampled from a series of Rayleigh wave group velocity maps for different periods, which are developed from surface wave dispersion measurements from local earthquakes (Supplemental Figure 1).

For input to the surface wave inversion, period-dependent Rayleigh wave group velocities are measured for 133 $M \geq 3.5$ earthquakes, excluding any within the Bucaramanga nest. To prepare the raw waveforms, the station response is removed from 26-minute segments of vertical-channel data, producing displacement time series. Forty-two stations are included in the surface wave analysis, as responses are not available for some stations and other stations are too short-period to yield useful data. Using the multiple-filter analysis program PGSWMFA [available at eqseis.geosc.psu.edu/~cammon/TOOLS/CJA_SWMFA.tar.gz], Rayleigh wave group velocities are measured at a range of periods. Only dispersion curves with signals above the USGS high-noise curve [Peterson, 1993] and with smoothly varying velocities over varying period are considered.

The Rayleigh wave measurements are then inverted for a period-dependent velocity model with a 0.5° node spacing, 1-second intervals in period, and smoothing between periods [Cho et al., 2007]. A range of damping, lateral smoothing, and inter-period smoothing values are tested, and the optimal combination is obtained using L-curve analysis [Aster et al., 2012]. The resulting model is sampled at the horizontal nodes used in the joint inversion (Figure 2) to obtain a Rayleigh wave group velocity dispersion curve for each node. At any given node, only the periods that are sampled by at least 10 rays at that location are considered. In the absence of a well-constrained velocity for a given period, nothing is used, resulting in measurements for periods between 10 sec and 70 sec.

2.3 Gravity

Gravity data originate from the Earth Gravitational Model 2008 (EGM2008) of Pavlis et al. [2012], which uses data from the Gravity Recovery and Climate Experiment (GRACE) satellite mission to develop a spherical harmonic model of Earth's gravitational potential. For ease of use, the model is accessed in the form of Bouguer anomalies [Fullea et al., 2008; Supplemental Figure 2] in geographic coordinates from the Bureau Gravimétrique International (bgi.omp.obs-mip.fr, accessed June 2, 2014). The gravity data are resampled at the horizontal node locations for use in the joint inversion.

3. Joint Inversion Method

The joint inversion method is based on the body-wave velocity tomography algorithm tomoDD [Zhang and Thurber, 2003, 2006], with surface wave dispersion curves and gravity data included to directly constrain the P- and S-body wave velocity model. This method builds upon those described in Zhang et al. [2014] and Maceira and Ammon [2009].

3.1 Body wave component

As is common in a linearized travel-time regional velocity inversion, P- and S-wave arrival times are used to iteratively perturb a starting velocity model and obtain a 3D velocity model that better fits the data, with rays retraced in the perturbed velocity model in each iteration. The earthquake hypocenters are first located in the 1D starting velocity model, and they are adjusted simultaneously with velocity during the iterations of the inversion. The absolute arrival times are weighted most heavily in early iterations, with a higher weight placed on relative arrival times in subsequent iterations in order to first constrain the coarse features of the velocity model and seismicity distribution before refining the details.

A significant improvement in the algorithm over earlier joint versions [Zhang et al., 2014; Syracuse et al., 2015] is the use of a modified pseudo-bending ray tracer, which is appropriate for use over a wide range of scales, from local to global [Um and Thurber, 1987; Koketsu and Sekine, 1998; Pesicek et al., 2010]. This modification reduces the time spent on ray tracing, the slowest part of the algorithm, by approximately 67% in comparison to a finite-difference ray tracer [e.g., Hole and Zelt, 1995], with negligible effect on the results.

3.2 Surface wave component

Surface wave dispersion measurements are primarily sensitive to Vs. Theoretically, the dispersion curve is a nonlinear function of Vs, Vp, and the density of the media [Bucher and Smith, 1971]. However, the sensitivity to Vp is significantly smaller than the sensitivity to Vs [Takeuchi and Saito, 1972; Aki and Richards, 1980], and the sensitivity to density is also smaller than to Vs [Bache et al., 1978; Tanimoto, 1991]. Therefore we only relate the surface wave dispersion observations to shear velocity variations, and we do not consider the effect of surface waves in solving for Vp variations, following Julià et al. [2000]. We follow Maceira and Ammon [2009] for the implementation of the dependency between Vs and surface wave dispersion observations.

3.3 Gravity component

Gravity is linked to Vp and Vs following the method described in Maceira and Ammon [2009], but using the relation between velocity and density of Ludwig et al. [1970], as implemented by D. G. Harkrider (personal communication, 2010). For simplicity in the gravity calculation, each node is considered to be surrounded by a constant-density volume, versus a continually varying-density volume.

Unlike the surface wave dispersion curves, which are only affected by velocities directly below the node, the gravity at given location is also affected by surrounding nodes. Here, neighboring nodes within 200 km horizontally of a target node are considered to contribute to the gravity anomaly at that node. Beyond this distance, neighboring nodes have a small effect. To remove long-wavelength features in the gravity data, which are mainly caused by deep density variations or non-isostatically compensated structures, while preserving sharp boundaries, the gravity data are filtered by removing the mean gravity value calculated at nodes within 2° of the target node. Correspondingly, gravity-based partial derivatives contributing to the velocity at a target node are filtered by removing the mean gravity partial derivative within 2° of the contributing node.

3.4 Running the inversion and its effects

Due to the differing sensitivities of each dataset, an initial model that fits one type of data may not fit another well. In order to fit the gravity data and shorter-period dispersion measurements, a vertical grid spacing of 5 km is used, which is smaller than might typically be used when only inverting body wave measurements. Similarly, the model also extends significantly deeper than the deepest seismicity (500 km) in order to fit longer-period surface waves, although the surface waves have little effect on the velocities at these deeper nodes during the inversion.

Here, the 1D model developed by Ojeda and Havskov [2001] for Colombia using local P- and S-wave data, combined with an assumed Vp/Vs of 1.78, results in predicted Rayleigh wave velocities that are up to 0.25 km/s faster than the mean Rayleigh wave group velocity between 10 and 70 sec. However, the local body waves provide limited constraint on velocities in the shallowest layers between stations. We obtain a 1D starting model that both better fits the surface waves and does not degrade the fit to the arrival time data (Figure 4) by jointly inverting P- and S-arrival times and a dispersion curve representing the average for the entire region for a 1D Vp and Vs model. This model is adjusted slightly to ensure that both Vp and Vs increase monotonically in depth, and it is then extended to three dimensions, with a horizontal grid spacing of 50 km. We do not include a high-velocity slab in the starting model in order to prevent bias in the final model toward an assumed slab geometry.

As in any damped or smoothed inversion, one must explore a range of regularization parameters in order to obtain an optimal model (Figure 5). Here, the relative weights of the different data types must also be explored. To efficiently determine the optimal values of these parameters, the damping and smoothing values are first chosen from L-curve analysis of model length and root-mean squared (RMS) residuals for a suite of inversions using only body waves, as body wave derivatives comprise the majority of the partial derivative matrix (Figure 5a-b). After the optimal damping and smoothing combination is identified, a range of surface wave and gravity weights are explored while holding the body wave weight, damping, and smoothing fixed (Figure 5c-k). The optimal combination of data weights is identified as the one that produces the largest improvement in RMS residual for each data type relative to the smallest RMS residual possible for that data type with the given model parameterization (e.g., an RMS misfit of zero is impossible for body wave arrivals). Assuming a body wave weight of 1, the optimal set of regularization parameters and data weights are: damping=300, smoothing=150, surface wave weight=3.0, gravity weight=0.05 (Figure 5).

Several interesting factors concerning the behavior of the joint inversion, as an effect of the parameterization, are noted. For example, within the range of data weights tested, adding surface waves and gravity to the inversion increases the RMS misfit to the body wave data, as would be expected, but only by a modest amount in comparison to when increasing the damping or smoothing in a body-wave-only inversion (Figure 5a-e). Even small weights applied to the gravity data dramatically improve the ability of the model to fit the data (Figure 5i-j). Although the surface waves do not directly affect the Vp model in the inversion, there is a tendency for larger surface wave weights to result in larger Vp models (Figure 5g).

The use of multiple datasets in the joint inversion has a range of effects on the resulting velocity model (Figures 6, 7). Supplemental Figure 3 compares the velocity models from a body-wave-only inversion, an inversion of body waves and surface waves, an inversion of body waves and gravity data, and the inversion using all three datasets discussed throughout this paper.

The surface wave and gravity data directly influence the shallower layers of the models. Surface waves help establish Vs over broad distances in the upper ~70 km, while the gravity data tend to enhance lateral contrasts in both Vp and Vs. The surface waves do not directly affect the Vp derivatives in the inversion, but their inclusion does influence the hypocenters through their effect on Vs, which tends to result in a smoother crustal Vp model. Although both the surface waves and gravity affect the shallow layers most strongly, their inclusion also affects velocities below 100 km depth. This is likely due to their assistance in properly attributing crustal travel time perturbations to the shallower portions of the model, which then improves the velocity recovery in deeper portions of the model. This can be seen in the difference in the recovery of fast velocities of the slab both in the actual inversion (Supplemental Figure 3) and in the velocity recovery tests (Figure 8, Supplemental Figure 4; discussed in Sections 4.2 and 5.1.1).

Occasionally, body-wave tomographic models include seemingly erroneous velocity perturbations that only span a node or two. This most often occurs near the edge of a model, associated with poor raypath coverage, but similar features may also be observed in the interior of a model. They are usually considered artifacts when near the edge of a model, but it is unclear whether they are real when in the interior of a model. Here, we find a significant reduction in this type of anomaly in the joint inversion. Near the edges of body wave coverage, these anomalies are unsupported by other datasets and are removed, while some small anomalies in the interior of the model are supported by other datasets and remain, implying that they are real features of the earth.

4. Results

4.1 Hypocenters

In comparison to the RSNC catalog locations, the relocations our 3D velocity model move, on average, 6 km deeper, with a negligible average epicentral shift. Shallower than 50 km depth, seismicity is organized into several features, much of which corresponds to previously identified crustal faults (Figure 1, 2) and is discussed in Section 5.2.

Below 50 km depth, the nature of slab seismicity varies along strike (Figures 3, 6, 7). In the Cauca segment, seismicity spans a ~40-km-wide Wadati-Benioff zone. There is evidence of a bimodal distribution that resembles the double seismic zones observed in many other slabs, although the separation between the two possible layers of seismicity observed here (30 km) is much larger than would be expected for a subducting plate of such a young age (11-17 Ma at the trench [Syracuse and Abers, 2006]) [Brudzinski et al., 2007]. In this segment, the slab seismicity dips at 40° at 100 km depth. South of 3° N, recorded slab seismicity is sparse due to few nearby seismic stations in Colombia.

In the Bucaramanga segment, we consider the slab seismicity north and south of 7.5° N separately. The southern section contains the Bucaramanga nest centered at (73.13° W, 6.82° N) (Figure 2, 7), where slab is clearly delineated by a 10-15 km thick layer of seismicity between 135 and 155 km depth. Within the study period, the largest earthquake in the Bucaramanga nest had a magnitude of 5.6 as reported by the RCSN. Here, the dip of the slab seismicity steepens significantly with depth, increasing from 10-30° shallower than 100 km depth, to 40-50° at 100 km depth, and to 60° below 100 km depth (Figure 7).

In addition to the Bucaramanga nest, we note multiple other clusters of seismicity in the Bucaramanga segment (Figure 3). Although these clusters are not as active as the Bucaramanga nest, they are clearly more active than other areas of the Bucaramanga and Cauca slab segments, and each is active throughout the study period. The most dominant cluster contains 53 earthquakes that form a streak elongated down-dip. It is centered at (73.76° W, 5.29° N) between 140 and 150 km depth (Figure 7, cluster 1), with a largest earthquake of M4.3. Three additional clusters contain 13 or fewer earthquakes each, with magnitudes 4.4 and below, and span much smaller areas. They are centered at (73.62° W, 6.35° N) between 105 and 115 km depth, at (73.53° W, 6.55° N) between 108 and 113 km depth, and at (73.19° W, 7.44° N) between 124 and 130 km depth (Figure 7, clusters 2-4, respectively). North of 7.5° N, slab seismicity is more scattered, and no clusters are apparent. Here, the slab dip is more constant over depth, with an average dip of 30-40°.

4.2 Velocities

P- and S-wave velocities (Figures 6, 7, Supplemental Figure 3) are recovered in the upper 200 km of the model, and we focus on interpreting them with respect to upper plate crustal structure, and slab and mantle wedge velocities of the subduction zone. Recovered crustal velocities vary over shorter length scales for Vp than Vs, which corresponds to the longer-wavelength sensitivity of the surface waves. Below 100 km depth, a high-velocity slab, 6% faster than the starting model in Vp and 4% faster in Vs, is clearly imaged in the Cauca segment at 85 km depth and below, while only deeper portions of the Bucaramanga slab segment are clear.

A series of synthetic recovery trials are conducted in order to assess which regions of the model may be well-recovered. While checkerboard models are often utilized for this type of a test, these models are highly unrealistic, and the polarity reversals in depth prove problematic when gravity data are included in the inversion. Gravity data place strong constraints on lateral changes in velocity, but they have limited constraint on velocity changes in depth. Although the gravity data and partial derivatives are filtered to reduce their effects on the model below the crust, their effect is not removed entirely, particularly in areas of the model that are not constrained by other data, which causes vertical smearing in checkerboard tests that is not evident in the inversion of real data.

As an alternative way of assessing recovery within the model, we test the recoveries for a suite of 100 random models. In each test, velocities are randomly perturbed in three dimensions up to ±7.5% from the 1D starting model; synthetic body wave, surface wave, and gravity data are calculated, with noise distributions following those of the real datasets; and the inversion is run using the optimal set of parameters identified in Section 3.4. For each pair of input and recovered models, we calculate the semblance based on Zelt [1998]. The 3D semblance distributions are averaged for the 100 models, and regions with an average semblance of 0.8 are identified as well-recovered parts of the model, and interpretations of velocities are limited to these regions. A comparison of the average semblance distributions for Vp and Vs for both body-wave-only and joint inversions is shown in Supplemental Figure 4.

5. Discussion

5.1 Subduction implications

5.1.1 Slab segmentation and flat subduction

The ~250 km offset in slab seismicity and reduced P-wave velocities between the high-velocity Bucaramanga and Cauca slab segments strongly suggest that the two segments are not connected below 100 km depth (Figure 6). Three synthetic tests of the recovery of a continuous slab, two overlapping slabs, or two non-overlapping slabs (Figure 8) indicate that the velocity pattern recovered here is consistent with the third scenario of two separate, non-overlapping slabs with a low-velocity mantle wedge above the Cauca slab segment, similar to the interpretations of Chiarabba et al. [2015], Vargas and Mann [2013], and Zarifi et al. [2007].

The complete separation of the Bucaramanga and Cauca slab segments below 50-100 km depth is also supported by other seismic, geodynamic and petrologic constraints. SKS splitting measurements by Porritt et al. [2014] show generally trench-perpendicular fast directions beneath the Central Cordillera and surrounding the Cauca segment, with a distinct rotation to trench-parallel fast directions near the southern edge of the Bucaramanga segment. While the patterns of anisotropy can be complex even in cases of simple two-dimensional corner flow, the fast direction of mantle anisotropy should be parallel to mantle flow in all areas except for the high-stress, low-temperature forearc corners of subduction zones [Jung and Karato, 2001; Kneller et al., 2005]. The fast-direction rotation observed between the Bucaramanga and Cauca slab segments by Porritt et al. [2014] indicates complex three-dimensional flow near the boundaries of the Bucaramanga and Cauca slab segments, corresponding to predicted anisotropy patterns for mantle flow around the edge of a slab [Jadamec and Billen, 2010].

Adakitic samples from Nevado del Ruiz Volcano [Borrero et al., 2009], located near the northern edge of Cauca slab seismicity, also support the interpretation of a slab tear or edge. Adakitic rocks are produced by the melting of subducted oceanic crust, which can occur when the slab is either young and warm [Defant and Drummond, 1990] or is heated via mantle flow around a slab edge (e.g., central Aleutians and Kamchatka [Yogodzinski et al., 2001], Costa Rica [Abratis and Wörner, 2001], eastern Alaska [Preece and Hart, 2004]). While the subducting crust in Colombia is indeed young and warm, thermal modeling of the subduction zone shows that a predominantly two-dimensional structure is unable to produce temperatures sufficient to melt subducted crust [Syracuse et al., 2010]; flow around the slab edge must play a large role in creating these melts.

These separate pieces of evidence, combined with our velocity model, clearly indicate a separation between the Bucaramanga and Cauca slab segments below 50-100 km depth. Projecting the two subducted segments back to the surface along the direction of convergence between the Nazca and South American plates [Sella et al., 2002] indicates that both segments are likely to have a Nazca origin, and the offset between them is caused by a slab tear. Seaward of this tear is the Sandra ridge [Vargas and Mann, 2013] (also referred to as the Coiba transform fault [Sallarès et al., 2003]), which forms a zone of weakness in the Nazca plate, allowing it to tear upon subduction. Upper-plate deformation beginning 10-15 Ma [Dengo and Covey, 1993] gives a possible origin time of the lateral offset between the two segments, which may have been caused by collision of the Panama arc with the South American plate [Vargas and Mann, 2013] or by subduction of a buoyant volcanic ridge, which increased coupling between the South American plate and the Nazca slab/Bucaramanga segment north of the tear [Chiarabba et al., 2015].

The low dip angle of seismicity in the Bucaramanga segment between the surface and 100 km depth and the large horizontal distance between the Nazca trench and intermediate-depth seismicity indicates that the Bucaramanga segment is an area of flat-slab subduction (Figure 7, cross sections B, C). In contrast to Chiarabba et al. [2015], we do not image a clear high-velocity flat slab following the base of the upper plate crust. This source of this discrepancy cannot be definitely identified, as Chiarabba et al. [2015]

only show velocity perturbations, although it may be related differences in the 1D starting model in the two studies. However, seismicity relocated in our study indicates that the top of the Bucaramanga slab traverses 400-500 km sub-horizontally between the trench and before reaching below 50 km depth, which certainly supports the interpretation of a flat-slab geometry. Eastward of the flat-slab section, the slab dip gradually steepens with depth, and seismicity continues to a maximum depth of 160-190 km, depending of the location (Figure 7, cross sections B, C).

Immediately north of the Bucaramanga nest, a relative lack of slab seismicity between approximately 65 and 90 km depth begins to occur along the direction of convergence between the Nazca and South American plates, indicating that the slab below 90 km may not be continuous with the Nazca plate at shallower depths (Figure 7, cross section A). Additionally, differences in seismicity patterns north and south of 7.5° N (Section 4.1) may point to fundamental differences between the two portions of slab north and south of the Bucaramanga nest. We interpret this as an indication that the slab north of the Bucaramanga nest may have a Caribbean plate origin (Figure 9); we term the slab north of the Bucaramanga nest the Caribbean segment. However, we also note that in the Caribbean segment, the slab seismicity is not continuous between the Caribbean trench and 150 km depth. There are a variety of potential explanations for a lack of continuity in the seismicity near the base of the upper plate crust, including poorer station coverage in northernmost Colombia, resulting in omission of earthquakes from the RCSN catalog and increased hypocenter errors, relatively slow convergence between the Caribbean and South American plates resulting in a lower seismicity rate, and abnormal stress patterns within the Caribbean segment due to subduction of the Caribbean large igneous province [Hoernle et al., 2004]. It is also possible that tectonic tremor is present here, as is seen in a slab of a similar geometry in Mexico [Payero et al., 2008], although it has not yet been observed here.

5.1.2 The Bucaramanga nest

The intense seismicity of the Bucaramanga nest has been attributed to a variety of geometrical and thermal features of the subducting slab. Zarifi et al. [2007] modeled a similar slab geometry to that proposed here and found that stresses are highly concentrated where the edges of the Bucaramanga and Caribbean slabs interact.

Surrounding the Bucaramanga nest, we find reduced S-wave velocities, elevated P-wave velocities relative to surrounding nodes, but 0.1 km/s slower than Vp in the Cauca slab segment at similar depths (Figure 7, cross section B, Supplemental Figure 5). We caution that due to the different sensitivities of the Vp and Vs models, caused by both the inclusion of surface waves and the smaller size of the S-arrival dataset relative to the P-arrival dataset, calculating Vp/Vs from the separate Vp and Vs models is likely to produce erroneous features. However, since the polarities of the Vp, Vs, and Vp/Vs anomalies associated with the Bucaramanga nest are present in both the final joint model and the body-wave-only model, we conservatively interpret just the sign of the change in Vp/Vs surrounding the Bucaramanga nest. Compared to both the Vp/Vs in the 1D starting model and calculated for the Cauca slab segment at the same depths, the Bucaramanga nest is associated with an increase in Vp/Vs. This simultaneous increase in Vp/Vs and decrease in Vp indicates that melt or water may be present within the slab here [Hammond and Humphreys, 2000; Takei, 2002], or the nest may have locally elevated temperatures [Karato, 1993; Faul and Jackson, 2005]. These observations could be consistent with proposed mechanisms of intermediate-depth earthquakes of dehydration embrittlement [Kirby et al., 1996] and thermal shear runaway [Keleman and Hirth, 2007; Prieto et al., 2013].

5.1.3 Arc volcanism

The Bucaramanga-Cauca boundary also marks a north-south transition from non-volcanogenic to volcanogenic portions of the subduction zone. The majority of Earth's subduction zones produce arc volcanism, with notable exceptions of parts of Peru and Chile where flat slabs subduct shallowly or sub-horizontally below the upper plate crust [e.g., Syracuse and Abers, 2006; Hayes et al., 2012], as is observed here for the Bucaramanga slab.

At least two factors may contribute to the lack of volcanism in flat-slab systems: the hydration of the incoming plate and the thermal structure of the system. Flat slabs are often associated with locations of aseismic ridges and thickened incoming plate [e.g., Gutscher et al., 2000; Martinod et al., 2010] and may be linked to the subduction of a buoyant slab. Normal faulting within the slab as it bends and enters the trench has been observed through bathymetry, seismic reflection profiles, and earthquake focal mechanisms [e.g., Ranero et al., 2003; Emry and Wiens, 2015], and it provides a mechanisms for further hydration of the slab and the introduction of more water into the subduction system than is otherwise available. A thickened incoming plate that is resistant to bending at the trench may result in less slab hydration, potentially limiting melting the mantle wedge and arc formation. However, there is evidence of the opposite being true for the flat-slab section of Peru, where additional hydration causes the slab to be buoyant and release additional water to the mantle wedge than neighboring normally dipping portions of the slab [Kim and Clayton, 2015].

The second factor that may prevent volcanism is the thermal structure of the slab and mantle wedge. Comparing models for the Peru and Chilean flat slab sections to neighboring sections with similar incoming plate age, overlying plate, convergence velocity, and sediment thickness shows that flat slabs are ~50° warmer than more steeply dipping slabs at 100 km depth [Syracuse et al., 2010]. Assuming similar initial amounts of hydration, flat slabs lose up to 50% more water than more steeply dipping slabs between 80 and 100 km depth [van Keken et al., 2011]. The mantle wedge reaches temperatures sufficient for hydrous partial melting above a depth-to-slab of 100 to 150 km depth for both flat- and steeply dipping slabs, but the flat slabs have temperature gradients in the mantle wedge above the slab that are 10-15° lower than for more steeply dipping slabs in volcanogenic systems [Syracuse et al., 2010]. This reduced temperature gradient may result in a thicker thermal boundary layer that distributes slab-derived fluids over a larger volume in the mantle wedge, resulting in too low of a fluid concentration in the wedge to allow partial hydrous melting and volcanism.

The Caribbean segment is also non-volcanogenic, and although its shallow structure is poorly defined by seismicity, the horizontal offset between intermediate-depth seismicity in the southern Caribbean segment and the trench means that it should share a similar thermal structure to flat-slab subduction. Additionally, the increased thickness of the Caribbean large igneous province in comparison to typical oceanic crust would make it resistant to bending, normal faulting and hydration of the slab at the trench, similarly preventing mantle wedge partial melting.

The Cauca slab segment dips at a steeper angle more typical of volcanogenic subduction zones and is indeed volcanogenic. Due to the geometry of the RCSN, mantle wedge velocities are only recovered above the Cauca slab segment. Here, Vp and Vs are up to 5% and 3% slower, respectively, than the starting model, with average reductions of 1-3% and 1%, respectively, between 115 and 170 km depth. A comparison of the input and recovered velocities in the synthetic test containing two fast slabs and a slow mantle wedge above the Cauca segment shows that, on average, velocities within the Cauca wedge are recovered at 70% for Vp and 75% for Vs (Supplemental Figure 4).

According to relationships between temperature and velocity for dry olivine [Faul and Jackson, 2005], the observed reduction in Vp could imply that the wedge in the Cauca segment has an average temperature of approximately 1250° C, assuming an ambient mantle temperature of 1000° C. Additionally, laboratory measurements indicate that the presence of melt, as well as increased water content or temperature, should decrease Vp while increasing Vp/Vs [Hammond and Humphreys, 2000; Takei, 2002; Faul and Jackson, 2005]. Although the mantle wedge of the Cauca segment has a slightly lower Vp/Vs than our starting model, this is likely caused by differences in recovery between the Vp and Vs models. As the presence of an active volcanic arc above the Cauca segment necessitates subsurface melting, we interpret this reduction in Vp as caused by a combination of temperature and melt effects.

5.2 Upper plate features

5.2.1 Andes seismicity and crustal compensation

Seismicity within the South American upper plate is aligned with several known faults (Figures 1, 2). The most prominent example is the band of seismicity between the surface and 30 km depth, extending from 2-7° N through the center and at the eastern edge of the Eastern Cordillera. South of 4° N, a right-lateral fault cuts through the cordillera, while a series of reverse faults bound its eastern edge further north, often termed the Llanos fault system [Veloza et al., 2012]. While it is difficult to calculate focal mechanisms for these earthquakes due to few stations to their south or east and generally noisy P-wave onset polarities, the general patterns of onset polarities for these earthquakes confirm that their ruptures are likely consistent with right-lateral motion along these faults.

At 35 km depth, crustal velocities beneath the Eastern Cordillera are 3% lower for Vp and 2% lower for Vs, in comparison to those beneath the Western and Central Cordillera (Figure 6). This suggests that the Eastern Cordillera has a thicker crustal root than the Western and Central Cordillera, which is supported by receiver functions [Poveda et al., 2015]. This may indicate that the Eastern Cordillera is istostatically compensated, which the other two, younger, cordillera are not as well compensated.

5.2.2 Nazca versus South American plates

A notable result of including the surface wave data and the gravity data in the inversion is their ability to resolve a strong difference (5-9%) in both Vp and Vs between the slower, thick crust of the continental South America plate and the faster, young upper mantle of the oceanic Nazca plate in the upper 10-50 km of the model (Figure 6). When using both the body and surface wave datasets, this velocity contrast is observable only in Vs due to the lack of a direct relationship between surface waves and Vp in the inversion, while the contrast is observable in both Vp and Vs when using the body wave and gravity datasets. This again highlights the improvement in imaging capabilities when using multiple datasets.

5.2.3 Newly identified faults

Two faults that are not in a previous compilation of faulting in Colombia [Veloza et al., 2012] are identified from the crustal seismicity (Figures 1, 2). The first is oriented approximately N65E, extending from the western coast of Colombia near 6° N through the Western and Central Cordillera. This seismicity associated with this feature extends through the entire crust, from the surface to 50-60 km depth, with roughly 60% of the seismicity in the upper 20 km of the crust. Although it is difficult to calculate reliable focal mechanisms for these earthquakes, the patterns of P-wave onset polarities are consistent with right-lateral motion. Its orientation of 25° from the direction of convergence between South America and the extinct Panama island arc [Vargas and Mann, 2013], means that it is nearly optimally oriented to be accommodating motion between the two plates.

The second feature is a band of $M \leq 4$ seismicity, east of the RCSN at approximately (71.1-71.7° W, 3.8° N) with an orientation of N75W (Supplemental Figure 6). These earthquakes began in April 2013 and continued through at least March 2014 (the most recent seismicity analyzed in this study). They have been identified as the early part of a sequence of induced seismicity associated with increases in oil production at wells approximately 100 km SE of Puerto Gaitán [Gómez-Alba et al., 2015]. The seismicity tends to deepen to the east to 35 km depth, and it is relatively evenly distributed over time once it begins, with the exception of a near-vertical streak of seismicity in early 2014 at the western end of the band, which extends from the surface to 12 km depth. Given the position of the earthquakes relative to the network, it is possible that they began prior to 2013, but were not included in the RCSN catalog previously. However, no additional nearby stations were added around April 2013 (the closest station, PTGC, 100 km away, was added September 2013), and their onset coincides with an increase in oil production in late 2013/early 2013 [Gómez-Alba et al., 2015], so this apparent start date is likely real. Due to the obviously unfavorable position of this group of earthquakes relative to the network and their small magnitudes, their locations are relatively poorly constrained, particularly in depth and in the NW-SE directions, but a series of tests perturbing the initial locations of this seismicity indicates that the NW-SE elongation of the band is real. The P-wave onset polarities of these earthquakes prove inconclusive, but joint moment tensor and back-projection inversion indicates normal-faulting motion along a generally NW-SE fault, which would be consistent with rock collapse due to fluid removal [Gómez-Alba et al., 2015].

6. Conclusions

The earthquake relocations and velocity model obtained from joint inversion of body wave, surface wave, and gravity data place new constraints on the tectonics of the Colombian subduction zone. From north to south, we describe the subduction system as:

- Caribbean segment: shallowly dipping, non-volcanogenic subduction of the dry, buoyant Caribbean large igneous province beneath the South American plate.
- Bucaramanga segment: flat-slab, non-volcanogenic subduction of the Nazca plate, with the Bucaramanga nest influenced by interaction with the Caribbean segment.
- Cauca segment: steeply dipping, volcanogenic subduction of the Nazca plate, offset from the Bucaramanga segment due to tearing along the Sandra ridge and the collision of the Panama arc with the Bucaramanga segment or increased coupling between the Nazca and South American plates.

Several questions remain concerning subduction beneath Colombia, including: Do the Nazca and Caribbean slabs collide?; If so, does this cause the intense seismicity of the Bucaramanga nest?; If not, what are the locations and natures of the edges of the two slabs?

7. Acknowledgements

We thank the RSNC for providing us with the seismic data used in this study. Additional seismic data were obtained from the FDSN via IRIS, and gravity data were obtained from the Bureau Gravimétrique International. We also thank Editor P. Shearer, as well as two anonymous reviewers, for their comments on the manuscript. This work was supported by Los Alamos National Laboratory Director's Postdoctoral fellowship LDRD-

20130807PRD3, and under the auspices of the U.S. Department of Energy by Los Alamos National Laboratory under contract DE-AC52-06NA25396/LA15-SignalPropagation-NDD2Ab. This work was also part of the U.S. Department of Energy's crosscutting initiative on subsurface science and engineering (SubTER) and was partly supported by the US DOE's Fossil Energy-Coal Office through its Carbon Capture, Utilization, and Storage Program as managed by the National Energy Technology Laboratory's Strategic Center for Coal. The views and conclusions contained in this document are those of the authors and should not be interpreted as necessarily representing the official policies, either expressed or implied, of the U.S. Government.

References:

Abratis, M., and G. Wörner (2001), Ridge collision, slab-window formation, and the flux of Pacific asthenosphere into the Caribbean realm, *Geology*, *29*(2), 127-130.

Aki, K., and P. G. Richards (1980), Quantitative Seismology: Theory and Methods, 700 pp., W. H. Freeman, San Francisco, CA.

Aster, R. C., B. Borchers, and C. H. Thurber (2012), Parameter Estimation and Inverse Problems, 376 pp., Academic Press, Waltham, MA.

Bache, T. C., W. L. Rodi, and D. G. Harkrider (1978), Crustal structures inferred from Rayleigh-wave signatures of NTS explosions, *Bull. Seismol. Soc. Am.*, *68*, 1399-1413.

Borrero, C., L. M. Toro, M. Alvarán, and H. Castillo (2009), Geochemistry and tectonic controls of the effusive activity related with the ancestral Nevado del Ruiz volcano, Colombia, *Geofisica Internacional*, *48*(1), 149-169.

Brocher, T. M. (2005), Empirical relations between elastic wavespeeds and density in the

Earth's crust, *Bull. Seismol. Soc. Am.*, *95*, 2081-2092, doi:10.1785/0120050077.

Brudzinski, M. R., C. H. Thurber, B. R. Hacker, and E. R. Engdahl (2007), Global prevalence of double Benioff zones, *Science*, *316*(5830), 1472-1474, doi:10.1126/science.1139204.

Bucher, R. L., and R. B. Smith (1971), Crustal structure of the eastern Basin and Range Province and the northern Colorado Plateau from phase velocities of Rayleigh waves, in *The Structure and Physical Properties of the Earth's Crust*, Geophys. Monogr. Ser., vol. 14, edited by J. G. Heacock, pp. 59-70, AGU, Washington, D. C.

Chiarabba, C., P. De Gori, C. Faccena, F. Speranza, D. Deccia, V. Dionicio, and G. A. Prieto (2015), Subduction system and flat slab beneath the Eastern Cordillera of Colombia, *Geochem. Geophys. Geosyst.*, *17*, 16-27, doi:10.1002/2015GC006048.

Cho, K. H., R. B. Herrmann, C. J. Ammon, and K. Lee (2007), Imaging the upper crust of the Korean Peninsula by surface-wave tomography, *Bull. Seismol. Soc. Am.*, *97*(1B), 198-207, doi:10.1785/0120060096.

Corredor, F. (2003), Seismic strain rates and distributed continental deformation in the northern Andes and three-dimensional seismotectonics of northwestern South America, *Tectonophysics*, *372*, 147-166, doi:10.1016/S0040-1951(03)00276-2.

Cortés, M., and J. Angelier (2005), Current state of stress in the northern Andes as indicated by focal mechanisms of earthquakes, *Tectonophysics*, *403*, 29-58, doi:10.1016/j.tecto.2005.03.020.

Defant, M. J., and M. S. Drummond (1990), Derivation of some modern arc magmas by melting of young subducted lithosphere, *Nature*, *347*(6294), 662-665.

Dengo, C., and M. Covey (1993), Structure of the eastern cordillera of Colombia:

implications for trap styles and regional tectonics, *AAPG Bulletin*, *77*, 1315.

Du, W.-X., C. H. Thurber, and D. Eberhart-Phillips (2004), Earthquake relocation using cross-correlation time delay estimates verified with the bispectrum method, *Bull. Seismol. Soc. Am.*, *94*(3), 856-866, doi:10.1785/0120030084.

Emry, E. L., and D. A. Wiens (2015), Incoming plate faulting in the Northern and Western Pacific and implications for subduction zone water budgets, *Earth Planet. Sci. Lett.*, *414*, 176-186, doi:10.1016/j.epsl.2014.12.042.

Faul, U. H., and I. Jackson (2005), The seismological signature of temperature and grain size variations in the upper mantle, *Earth Planet. Sci. Lett.*, *234*(1-2), 119-134, doi:10.1016/j.epsl.2005.02.008.

Fullea, J., M. Fernandez, and H. Zeyen (2008), FA2BOUG - A FORTRAN 90 code to compute Bouguer gravity anomalies from gridded free-air anomalies: Application to the Atlantic-Mediterranean transition zone". *Compt. Geosci.*, *34*(12), 1665-1681, doi: 10.1016/j.cageo.2008.02.018.

Gómez-Alba, S., C. E. Fajardo-Zarate, and C. A. Vargas (2015), Stress field estimation based on focal mechanisms and back projected imaging in the Eastern Llanos Basin (Colombia), *J. South Am. Earth Sci.*, doi:10.1016/j.sames.2015.08.010.

Gutscher, M.-A., W. Spakman, H. Bijwaard, and E. R. Engdahl (2000), Geodynamics of flat subduction: Seismicity and tomographic constraints from the Andean margin, *Tectonics*, *19*(5), 814-833.

Hammond, W. C., and E. D. Humphreys (2000), Upper mantle seismic wave velocity: Effects of realistic partial melt geometries, *J. Geophys. Res.*, *105*(B5), 10,975-10,986, doi:10.1029/2000JB900041.

Hayes, G. P., D. J. Wald, and R. L. Johnson (2012), Slab1.0: A three-dimensional model of global subduction zone geometries, *J. Geophys. Res.*, *117*, B01302, doi:10.1029/2011JB008524.

Hoernle, K., F. Hauff, and P. van den Bogaard (2004), 70 m.y. history (139-69 Ma) for the Caribbean large igneous province, *Geology*, *32*(8), 697-700, doi:10.1130/G20574.1.

Hole, J. A., and B. C. Zelt (1995), 3-D finite-difference reflection traveltimes, *Geophys. J. Int.*, *121*, 427-434.

Jadamec, M. A, and M. I. Billen (2010), Reconciling surface plate motions with rapid three-dimensional mantle flow around a slab edge, *Nature*, *465*(7296), 338-341, doi:10.1038/nature09053.

Julià, J., C. J. Ammon, R. B. Herrmann, and A. M. Correig (2000), Joint inversion of receiver function and surface wave dispersion observations, *Geophys. J. Int.*, *143*, 99-112.

Jung, H., and S.-I. Karato (2001), Water-induced fabric transitions in olivine, *Science*, *293*, 1460-1463.

Karato, S. (1993), Importance of anelasticity in the interpretation of seismic tomography, *Geophys. Res. Lett.*, *20*(15), 1623-1626, doi:10.1029/93GL01767.

Keleman, P. B., and G. Hirth (2007), A periodic shear-heating mechanism for intermediate-depth earthquakes in the mantle, *Nature*, *446*, 787-790.

Kim, Y., and R. W. Clayton (2015), Seismic properties of the Nazca oceanic crust in southern Peruvian subduction system, *Earth Planet. Sci. Lett.*, *429*, 110-121, doi:10.1016/j.epsl.2015.07.055.

Kirby, S. H., S. Stein, E. Okal, and D. C. Rubie (1996), Metastable mantle phase transformations and deep earthquakes in subducting oceanic lithosphere, *Rev. Geophys.*, *34*, 261-306.

Kneller, E. A., P. E. van Keken, S.-I. Karato, and J. Park (2005), B-type olivine fabric in the mantle wedge: Insights from high-resolution non-Newtonian subduction zone models, *Earth Planet. Sci. Lett.*, *429*, 781-797, doi:10.1016/j.epsl.2005.06.049.

Koketsu, K., and S. Sekine (1998), Pseudo−bending method for three-dimensional seismic ray tracing in a spherical earth with discontinuities, *Geophys. J. Int.*, *132*, 339-346.

Ludwig, W. J., J. E. Nafe, and C. L. Drake (1970), Seismic refraction, in *The Sea,* vol. 4, edited by A. E. Maxwell, pp. 53-84, Interscience, New York.

Maceira, M., and C. J. Ammon (2009), Joint inversion of surface wave velocity and gravity observations and its application to central Asian basins shear velocity structure, *J. Geophys. Res.*, *114*, B02314, doi:10.1029/2007JB005157.

Malavé, G., and G. Suárez (1995), Intermediate-depth seismicity in northern Colombia and western Venezuela and its relationship to Caribbean plate subduction, *Tectonics*, *14*(3), 617-628.

Martinod, J., L. Husson, P. Roperch, B. Guillaume, and N. Espurt (2010), Horizontal subduction zones, convergence velocity and the building of the Andes, *Earth Planet. Sci. Lett.*, *299*, 299-309, doi:10.1016/j.epsl.2010.09.010.

Ojeda, A., and J. Havskov (2001), Crustal structure and local seismicity in Colombia, *J. Seismol.*, *5*, 575-593.

Pavlis, N. K., S. A. Holmes, S. C. Kenyon, and J. K. Factor (2012), The development and evaluation of the Earth Gravitational Model 2008 (EGM 2008), *J. Geophys. Res., 117*, B04406, doi:10.1029/2011JB008916.

Payero, J. S., V. Kostoglodov, N. Shapiro, T. Mikumo, A. Iglesias, X. Pérez-Campos, and R. W. Clayton (2003), Nonvolcanic tremor observed in the Mexican subduction zone, *Geophs. Res. Lett.*, *35*, L07305, doi:10.1029/2007GL032877.

Pennington, W. D. (1981), Subduction of the eastern Panama Basin and seismotectonics of northwestern South America, *J. Geophys. Res.*, *86*(B11), 10753-10770.

Pesicek, J. D., C. H. Thurber, H. Zhang, H. R. DeShon, E. R. Engdahl, and S. Widiyantoro (2010), Teleseismic double-difference relocation of earthquakes along the Sumatra-Andaman subduction zone using a 3-D model, *J. Geophys. Res.*, *115*, B10303, doi:10.1029/2010JB007443.

Peterson, J. (1993), Observations and Modeling of Seismic Background Noise, U.S. Geological Survey Open-File Report 93-322, 94 p.

Plouff, D. (1976), Gravity and magnetic fields of polygonal prisms and application to magnetic terrain corrections, *Geophysics*, *41*(4), 727-741.

Porritt, R. W., T. W. Becker, and G. Monsalve (2014), Seismic anisotropy and slab dynamics from *SKS* splitting recorded in Colombia, *Geophys. Res. Lett.*, *41*, 8775-8783, doi:10.1002/2014GL061958.

Poveda, E., G. Monsalve, and C. A. Vargas (2015), Receiver functions and crustal structure of the northwestern Andean region, Colombia, *J. Geophys. Res.*, *120,* 2408-2425, doi:10.1002/2014JB011304.

Preece, S. J., and W. K. Hart (2004), Geochemical variations in the <5 Ma Wrangell Volcanic Field, Alaska: implications for the magmatic and tectonic development of a complex continental arc system, *Tectonophysics*, *392*, 165-191, doi:10.1016/j.tecto.2004.04.011.

Prieto, G. A., G. C. Beroza, S. A. Barrett, G. A. López, and M. Florez (2012), Earthquake nests as natural laboratories for the study of intermediate-depth earthquake mechanics, *Tectonophysics*, *570*, 42-56, doi:10.1016/j.tecto.2012.07.019.

Ranero, C. R., A. Villasenor, J. P. Morgan, and W. Weinrebe (2005), Relationship between bend-faulting at trenches and intermediate-depth seismicity. *Geochem. Geophys. Geosyst.*, *6*(12), Q12002, doi:10.1029/2005GC000997.

Sallarès, V., P. Charvis, E. R. Flueh, and J. Bialas (2003), Seismic structure of the Cocos and Malpelo Volcanic Ridges and implications for hot spot-ridge interaction, *J. Geophys. Res.*, *108*(B12), 2564, doi:10.1029/2003JB002431.

Sanchez-Rojas, J., and M. Palma (2014), Crustal density structure in northwestern South America derived from analysis and 3-D modeling of gravity and seismicity data, *Tectonophysics*, *634*, 97-115, doi:10.1016/j.tecto.2014.026.

Schneider, J. R., W. D. Pennington, and R. P. Meyer (1987), Microseismicity and focal mechanisms of the intermediate-depth Bucaramanga nest, Colombia, *J. Geophys. Res.*, *92*(B13), 13913-13926.

Sella, G., T. H. Dixon, and A. Mao (2002), REVEL: A model of Recent plate velocities from space geodesy, *J. Geophs. Res.*, *107*(B4), 2081, doi:10.1029/2000JB000033.

Syracuse, E. M., and G. A. Abers (2006), Global compilation of variations in slab depth beneath arc volcanoes and implications, *Geochem. Geophys. Geosyst.*, *7*(5), Q05017, doi:10.1029/2005GC001045.

Syracuse, E. M., P. E. van Keken, and G. A. Abers (2010), The global range of subduction zone thermal models, *Phys. Earth. Planet. In.*, *183*(1-2), 73-90, doi:10.1016/j.pepi.2010.02.004.

Syracuse, E. M., M. Maceira, H. Zhang, and C. H. Thurber (2015), Seismicity and structure of Akutan and Makushin Volcanoes, Alaska, using joint body and surface wave tomography, *J. Geophys. Res.*, *120*(2), 1036-1052, doi:10.1002/2014JB011616.

Taboada, A., L. A. Rivera, A. Fuenzalida, A. Cisternas, H. Philip, H. Bijwaard, J. Olaya, and C. Rivera (2000), Geodynamics of the northern Andes: Subductions and intracontinental deformation (Colombia), *Tectonics*, *19*(5), 787-813.

Takei, Y. (2002), Effect of pore geometry on V_P/V_S: From equilibrium geometry to crack, *J. Geophys. Res.*, *107*(B2), 2043, doi:10.1029/2001JB000522.

Takeuchi, H., and M. Saito (1972), Seismic surface waves, in *Methods of Computational Physics*, edited by B. A. Bolt, pp. 217-295, Academic, New York.

Tanimoto, T. (1991), Waveform inversion for three-dimensional density and S-wave structure, *J. Geophys. Res.*, *96*, 8167-8189.

Um, J., and C. H. Thurber (1987), A fast algorithm for two-point seismic ray tracing, *Bull. Seismol. Soc. Am.*, *77*(3), 972-986.

van der Hilst, R., and P. Mann (1994), Tectonic implications of tomographic images of subducted lithosphere beneath northwestern South America, *Geology*, *22*, 451-454.

van Keken, P. E., B. R. Hacker, E. M. Syracuse, G. A. Abers (2011), Subduction factory: 4. Depth‐dependent flux of H2O from subducting slabs worldwide, *J. Geophys. Res.*, *116*, B01401, doi:10.1029/2010JB007922.

Vargas, C. A., L. G. Pujades, and L. Montes (2007), Seismic structure of south-central Andes of Colombia by tomographic inversion, *Geofísica Internacional*, *46*(2), 117-127.

Vargas, C. A., and P. Mann (2013), Tearing and breaking off of subducted slabs as the result of collision of the Panama arc-indenter with northwestern South America, *Bull. Seismol. Soc. Am.*, *103*(3), 2025-2046, doi:10.1785/0120120328.

Veloza, G., R. Styron, M. Taylor, and A. Mora (2012), Open-source archive of active faults for northwest South America, *GSA Today*, *22*(10), doi:10.1130/GSAT-G156A.1.

Waldhauser, F., and W. L. Ellsworth (2000), A double-difference earthquake location algorithm: Method and application to the northern Hayward fault, *Bull. Seismol. Soc. Am.*, *90*(6), 1353-1368.

Yarce, J., G. Monsalve, T. W. Becker, A. Cardone, E. Poveda, D. Alvira, and O. Ordoñez-Carmona (2014), Seismological observations in Northwestern South America: Evidence for two subduction segments, contrasting crustal thicknesses and upper mantle flow, *Tectonophysics*, *637*, 57-67, doi:10.1016/j.tecto.2014.09.006.

Yogodzinski, G. M., J. M. Lees, T. G. Chirikova, F. Dorendorf, G. Wöerner, and O. N. Volynets (2001), Geochemical evidence for the melting of subducting oceanic lithosphere at plate edges, *Nature*, *409*(6819), 500-504.

Zarifi, Z., J. Havskov, and A. Hanyga (2007), An insight into the Bucaramanga nest, *Tectonophysics*, *44*(1-2), 93-105, doi:10.1016/j.tecto.2007.06.004.

Zelt, C. A. (1998), Lateral velocity resolution from three-dimensional seismic refraction data, *Geophys. J. Int.*, *135*, 1101-1112.

Zhang, H., and C. H. Thurber (2003), Double-difference tomography: The method and its application to the Hayward Fault, California, *Bull. Seismol. Soc. Am.*, *93*(5), 1875-

1889, doi:10.1785/0120020190.

Zhang, H., and C. Thurber (2006), Development and applications of double-difference tomography, *Pure Appl. Geophys.*, *163*(2-3), 373-403, doi:10.1007/s00024-005-0021-y.

Zhang, H., M. Maceira, P. Roux, and C. Thurber (2014), Joint inversion of body-wave arrival times and surface-wave dispersion for three-dimensional seismic structure around SAFOD, *Pure. Appl. Geophys.*, *171*(11), 3013-3022, doi:10.1007/s00024-014-0806-y.

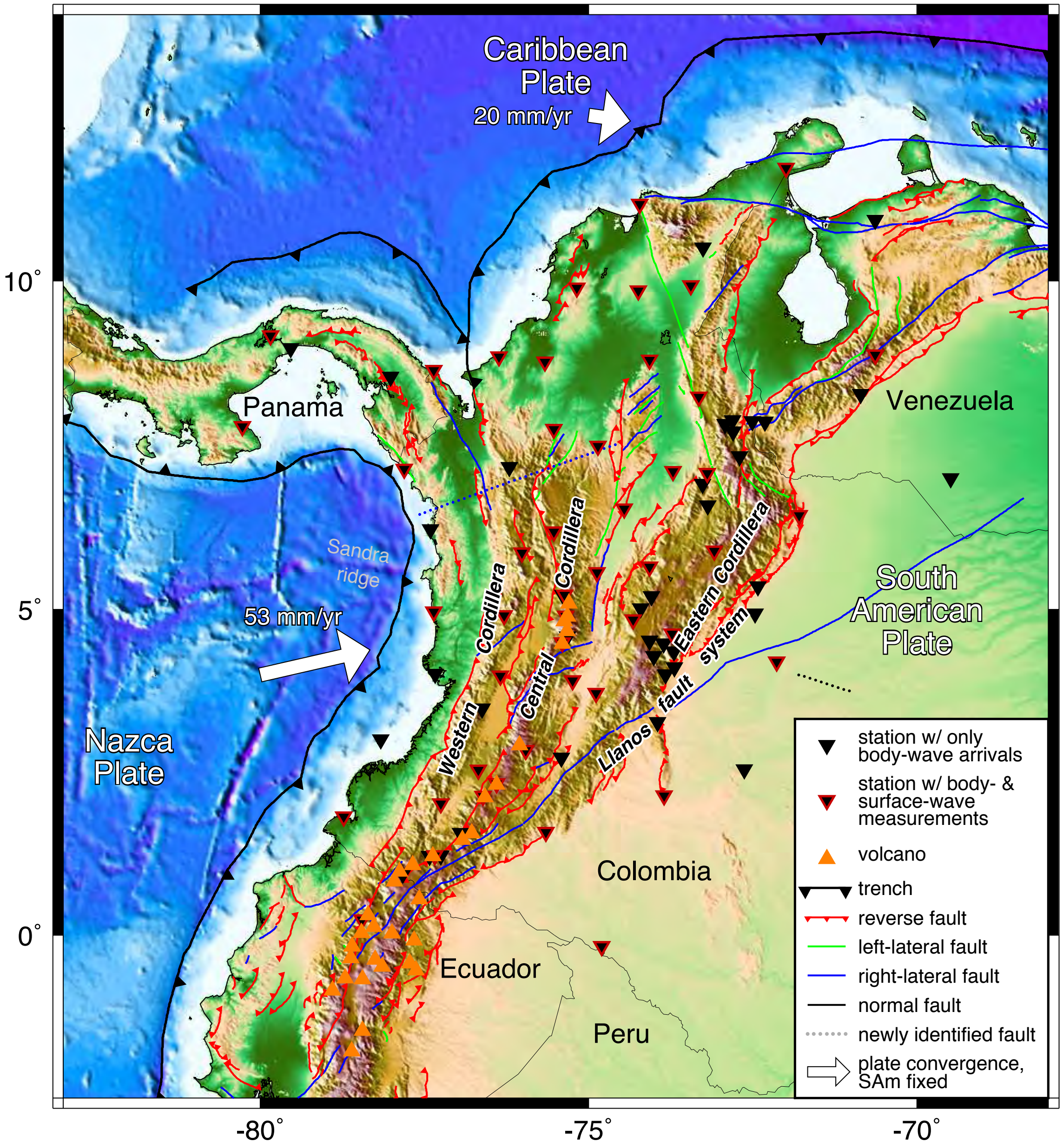

Figure 1. Overview map of the study area showing seismic station locations, faults [Veloza et al., 2012], including those newly identified in this study, and plate convergence vectors [Sella et al., 2002].

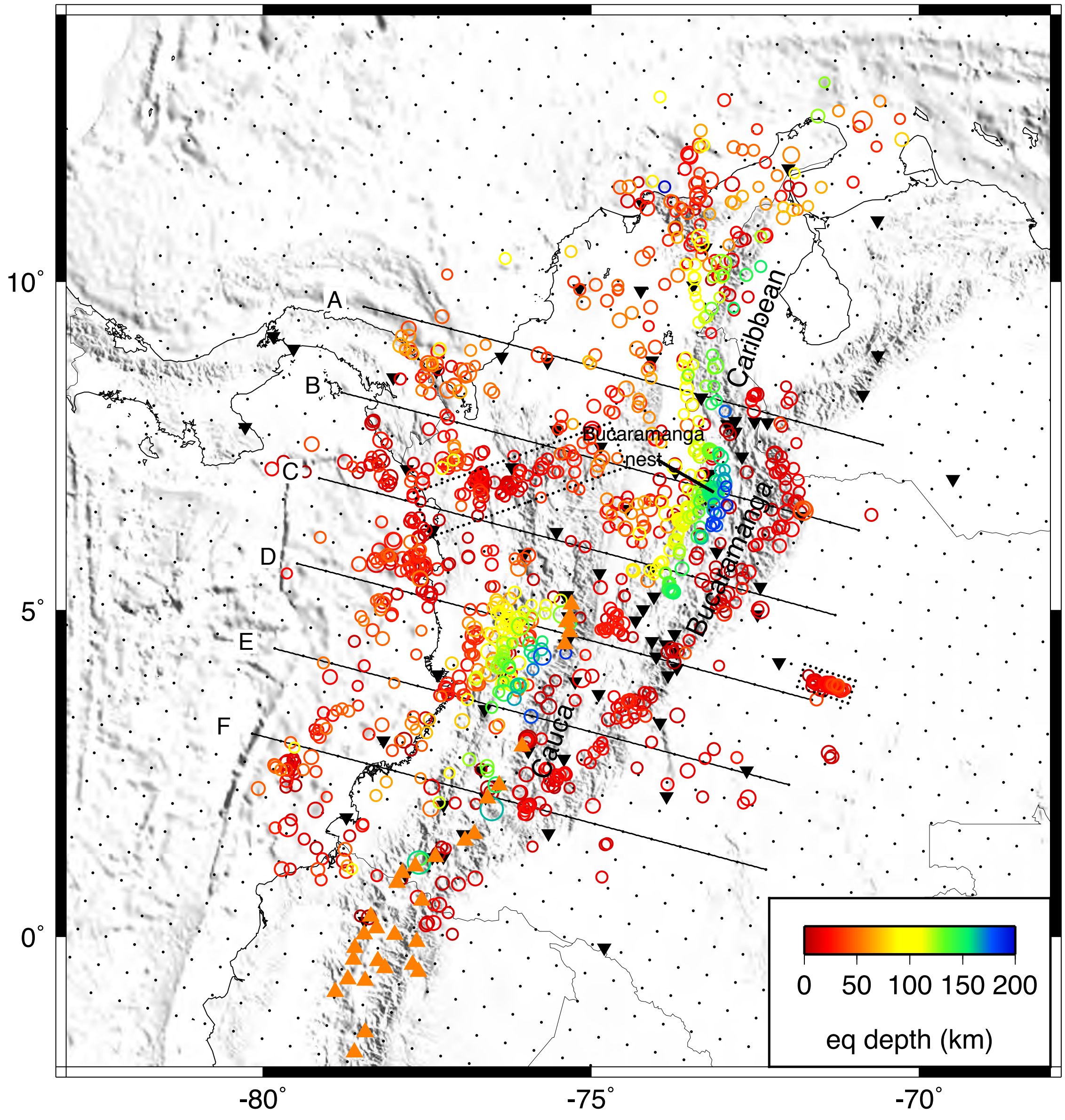

Figure 2. Map of relocated earthquakes, colored by depth and scaled by magnitude. Locations of the Caribbean, Bucaramanga and Cauca segments of the subduction zone and the Bucaramanga nest are indicated. Locations of grid nodes and of the cross sections shown in Figure 7 are indicated. Inverted triangles indicate station locations, and orange triangles indicate locations of arc volcanoes. Areas of seismicity associated with newly identified faults are outlined by dotted rectangles.

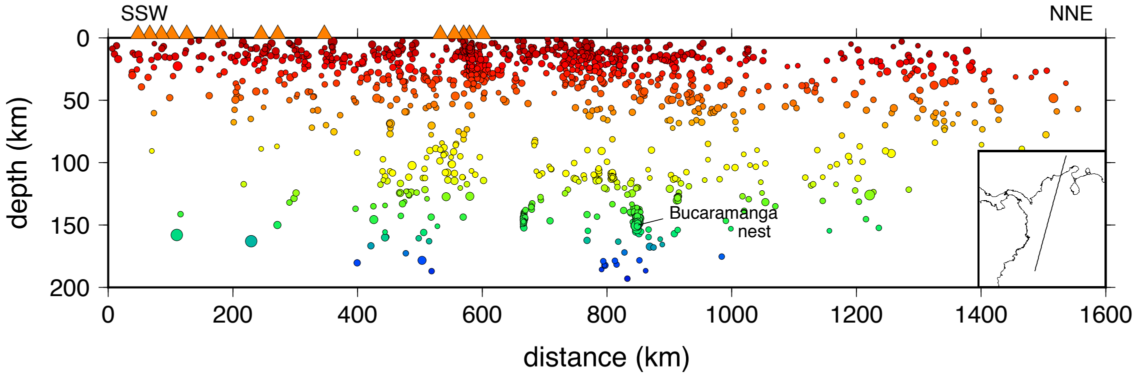

Figure 3. SSW-NNE cross-section of all relocated earthquakes, with inset showing the orientation of the projection, which follows that of the inversion grid, shown in Figure 2. Earthquakes are colored by depth and scaled by magnitude, and arc volcanoes are shown as orange triangles. Note the 2x vertical exaggeration.

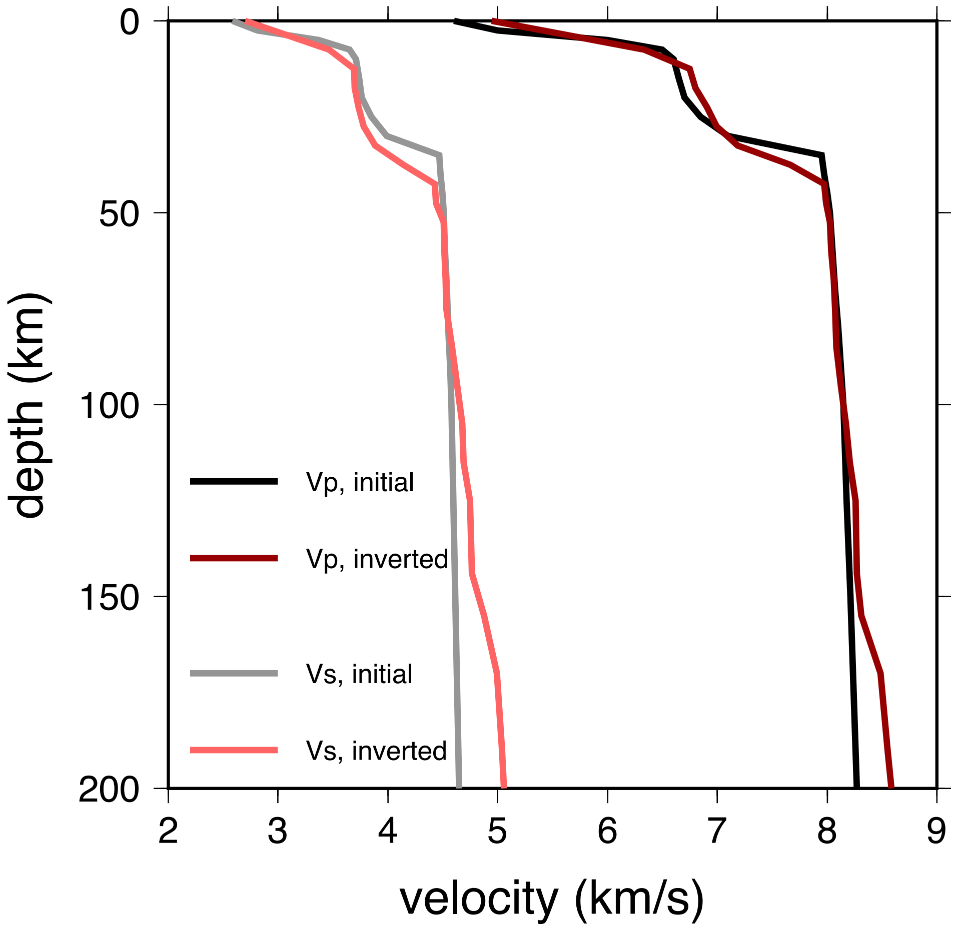

Figure 4.

Inverted Vp and Vs profiles from the 1D inversion of body wave and surface wave data and the initial Vp and Vs profiles based on Ojeda and Havskov [2001]. The inverted model is used as the starting model for the 3D inversion.

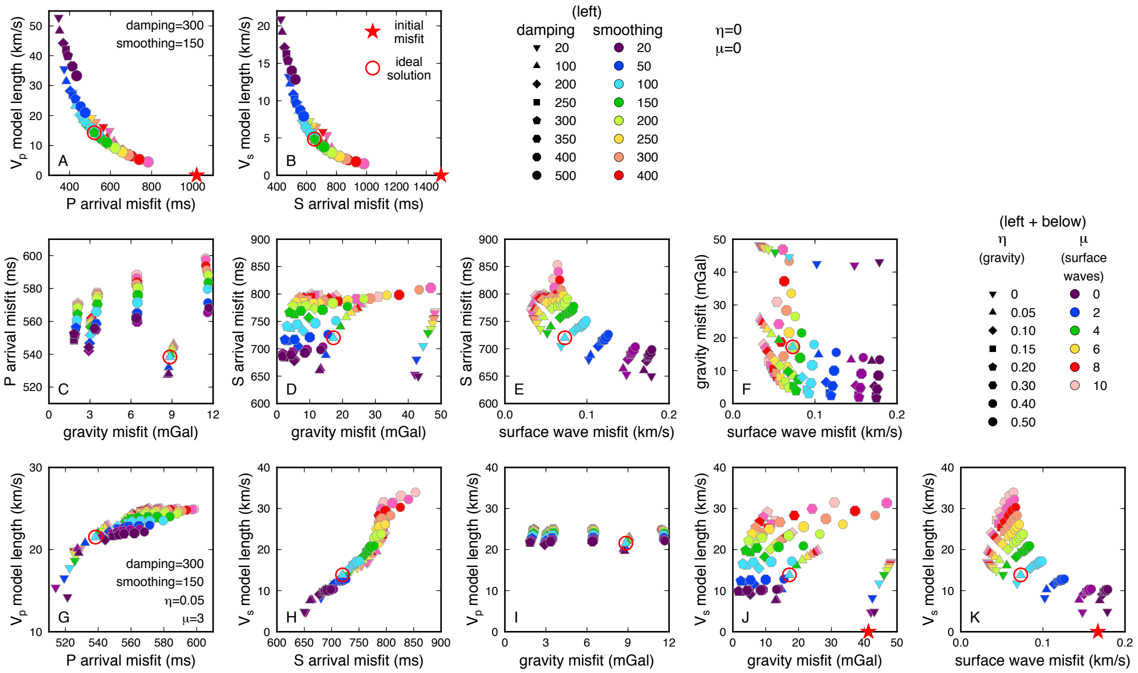

Figure 5. Tradeoff curves showing (top row) misfit versus model norm for a range of damping and smoothing values for the body-wave-only inversion; (middle row) comparisons of misfit for different datasets for the joint inversion, with a damping of 300 and smoothing of 150 held fixed; and (bottom row) misfit versus model length for each dataset in the joint inversion. For each panel, the results for the inversion with the optimized set of parameters is indicated by the red outlined circle. Initial misfits are indicated by the red star (gravity misfit to initial Vp model of 44 mGal is not shown).

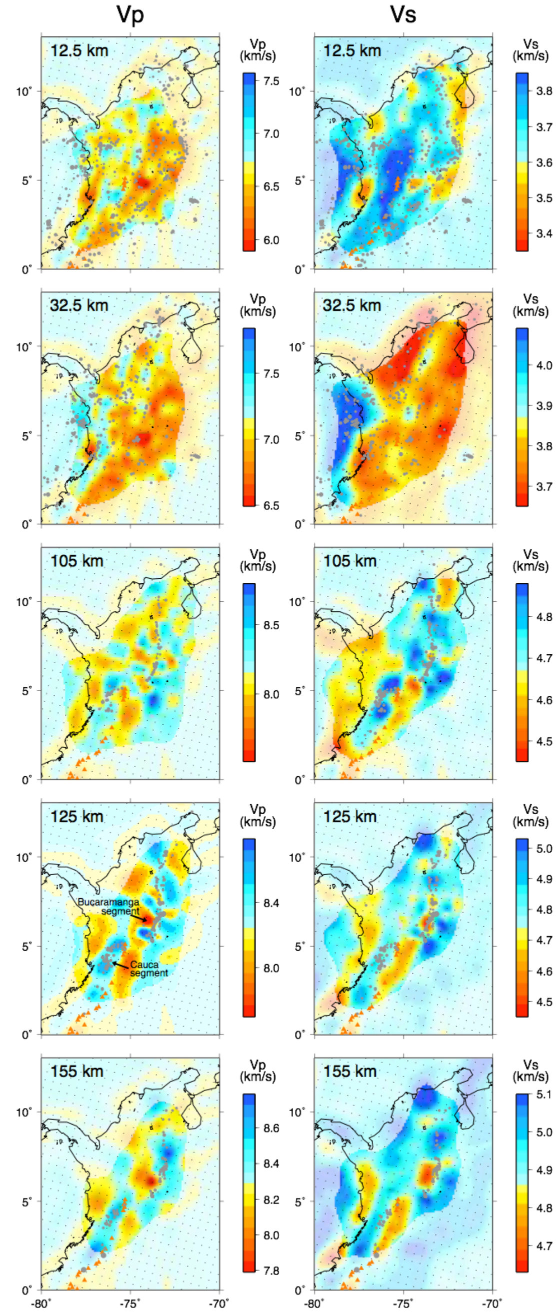

Figure 6. Maps of Vp and Vs for the joint inversion at selected depths. Gray circles show earthquake locations, and poorly recovered areas partially masked, based on semblance tests (Supplemental Figure 4, Section 4.2). For comparison of each combination of data types at all depths, refer to Supplemental Figure 3.

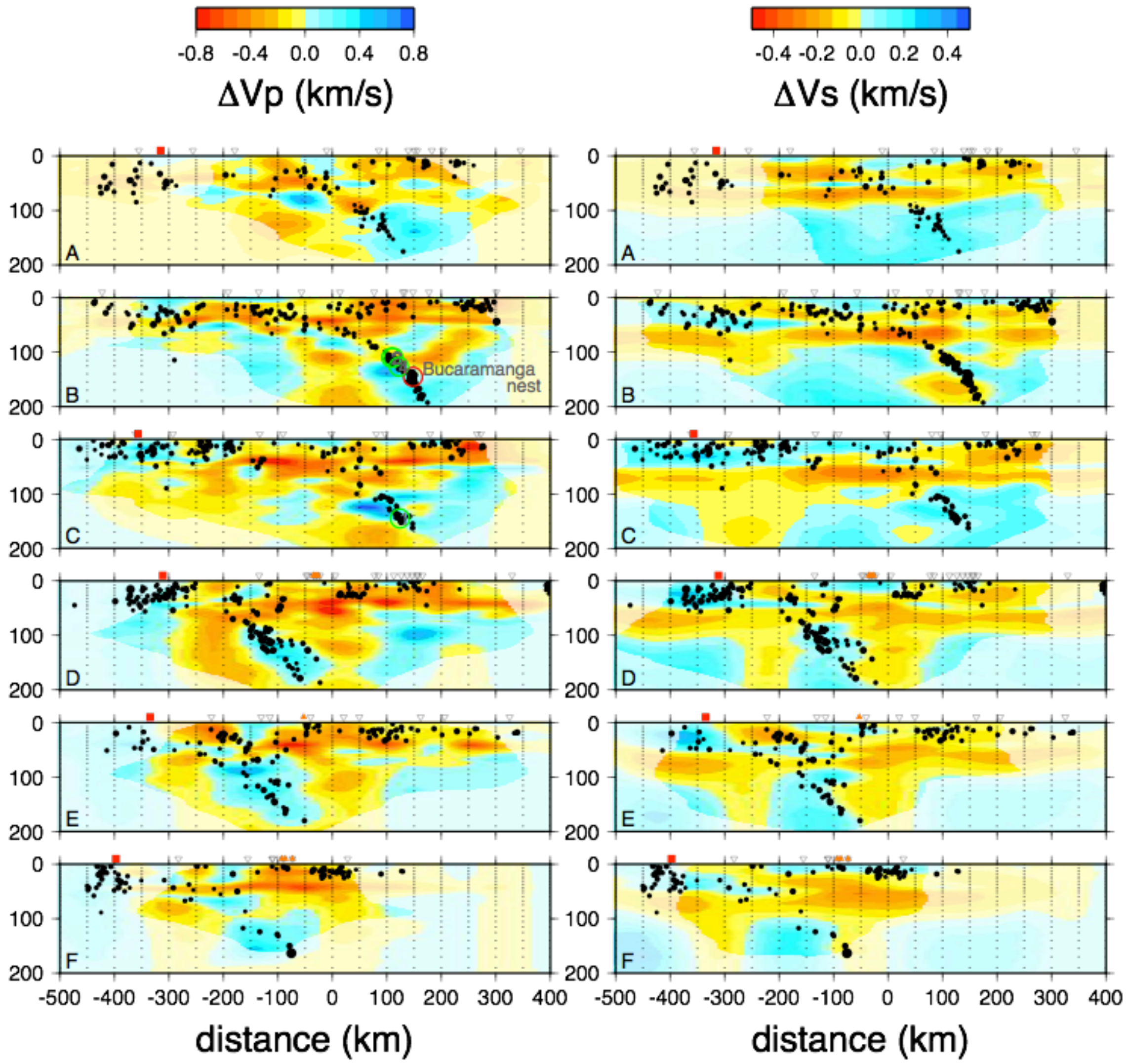

Figure 7. Cross sections showing Vp and Vs in the joint-inversion model, at locations indicated in Figure 2. Black circles show earthquake locations within 50 km of the profile, and poorly recovered areas are partially masked, based on semblance tests (Supplemental Figure 4, Section 4.2). The locations of the trench (red square), seismic stations (inverted triangles) and volcanoes (orange triangles) are shown. Locations of the Bucaramanga nest and clusters described in Section 4.1 are indicated on cross sections B and C. No vertical exaggeration.

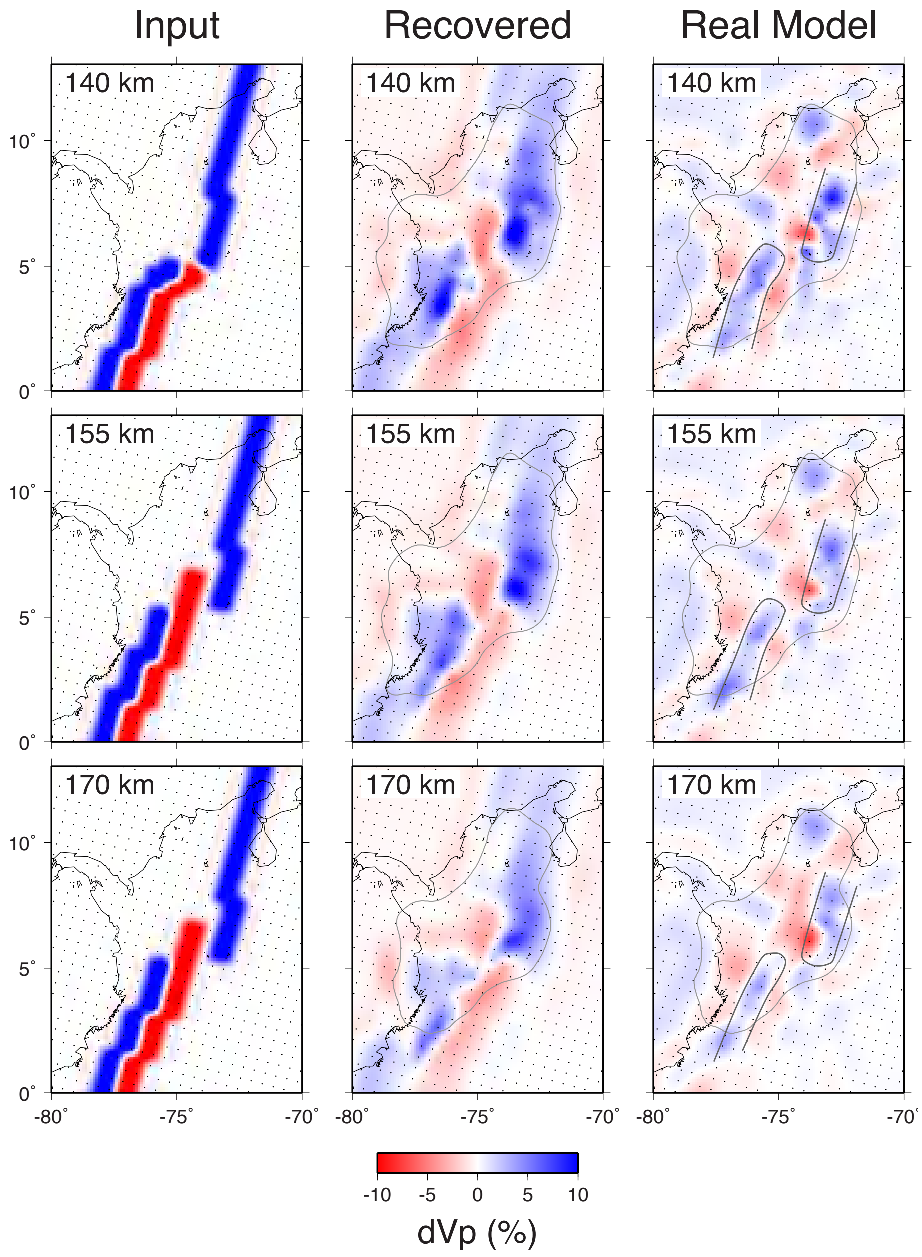

Figure 8. Comparison of an input synthetic velocity model showing a torn slab, the recovered Vp model, and the model using real data. Input slab anomalies are +10% in both Vp and Vs, and the input mantle wedge anomaly is -5%. Dark gray outlines encircle the approximate regions of interpreted slab location in the real model, and light gray outlines encircle the well-recovered portions of the model, based on semblance tests (see Supplemental Figure 4, Section 4.2).

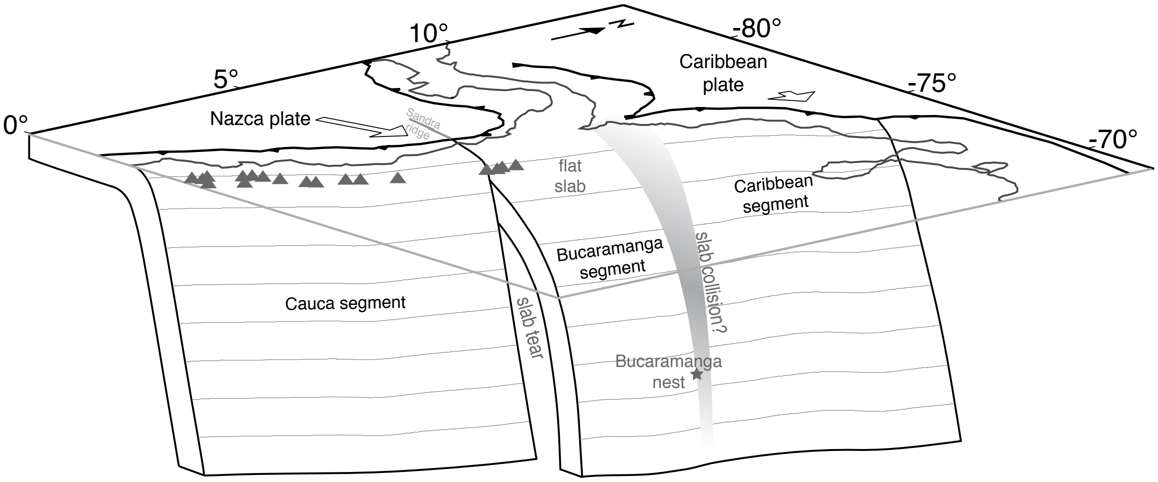

Figure 9. 3D schematic of the plate geometry proposed in this paper.

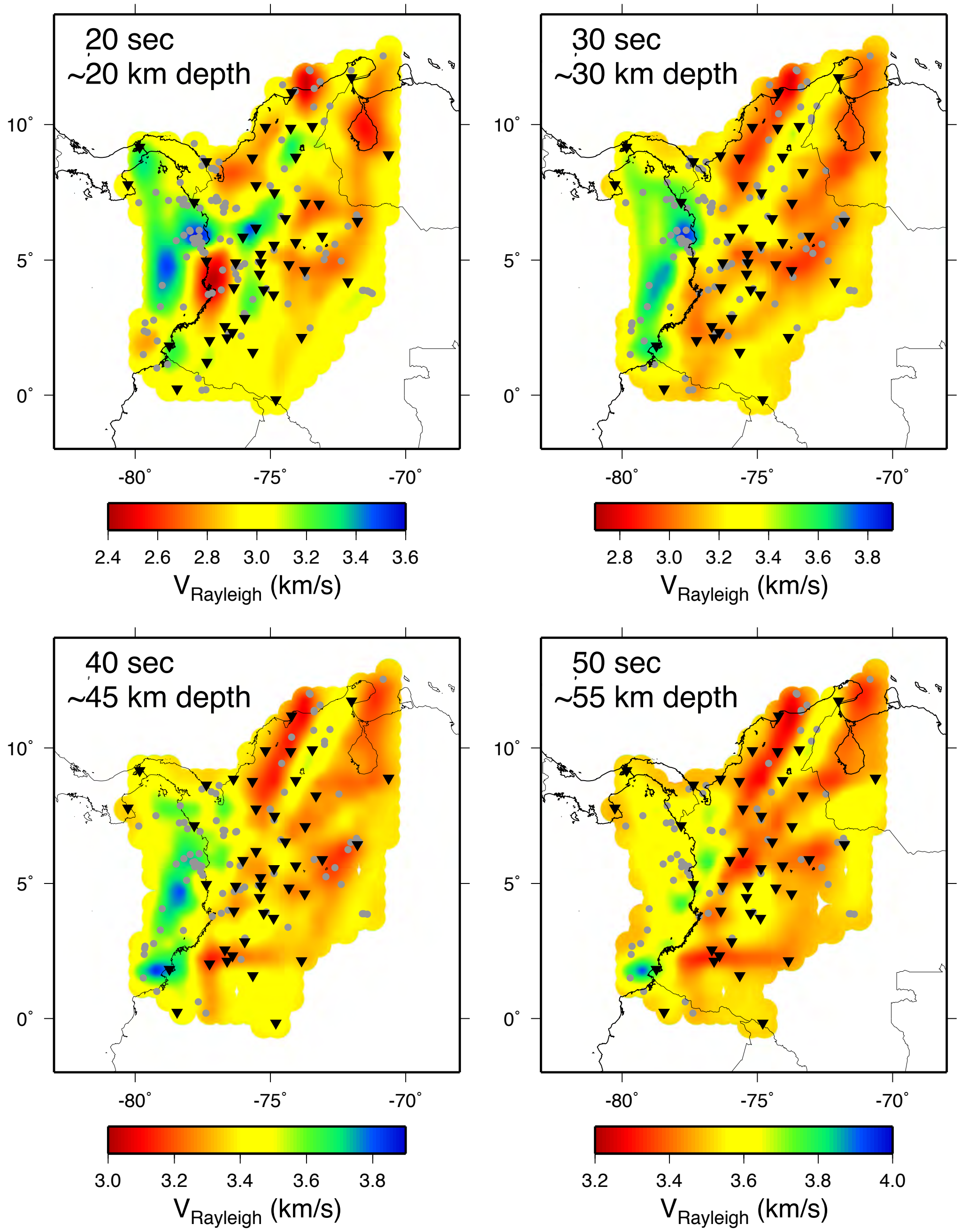

Supplemental Figure 1: Maps showing surface wave velocity at selected periods, with the approximate depth of maximum sensitivity indicated. Sources and stations sampling that particular period are shown as gray circles and black triangles, respectively.

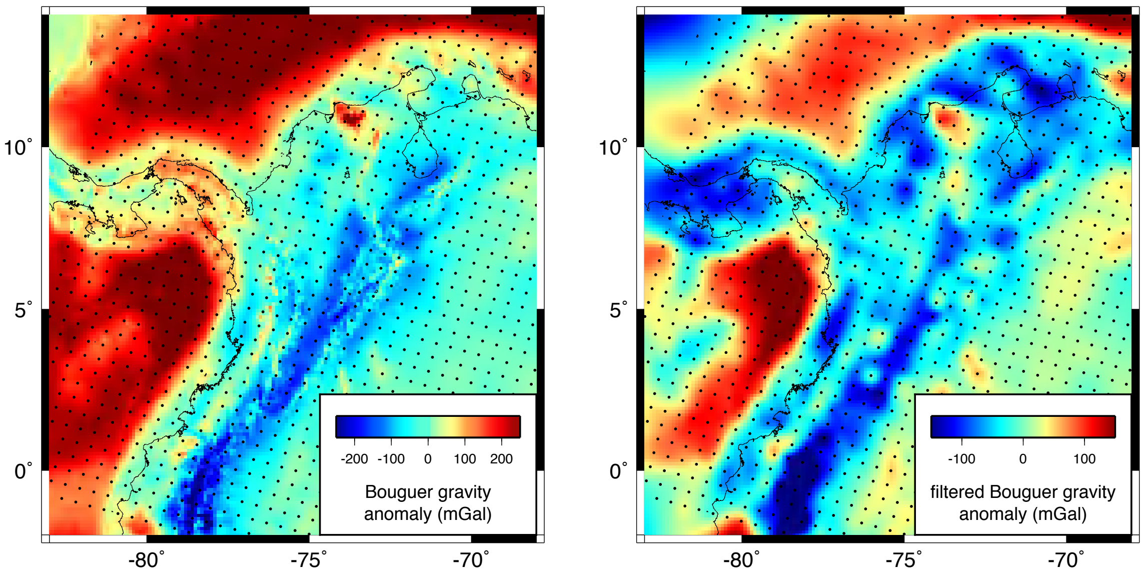

Supplemental Figure 2: Maps of (left) unfiltered Bouguer gravity data and (right) filtered Bouguer gravity data sampled at node locations.

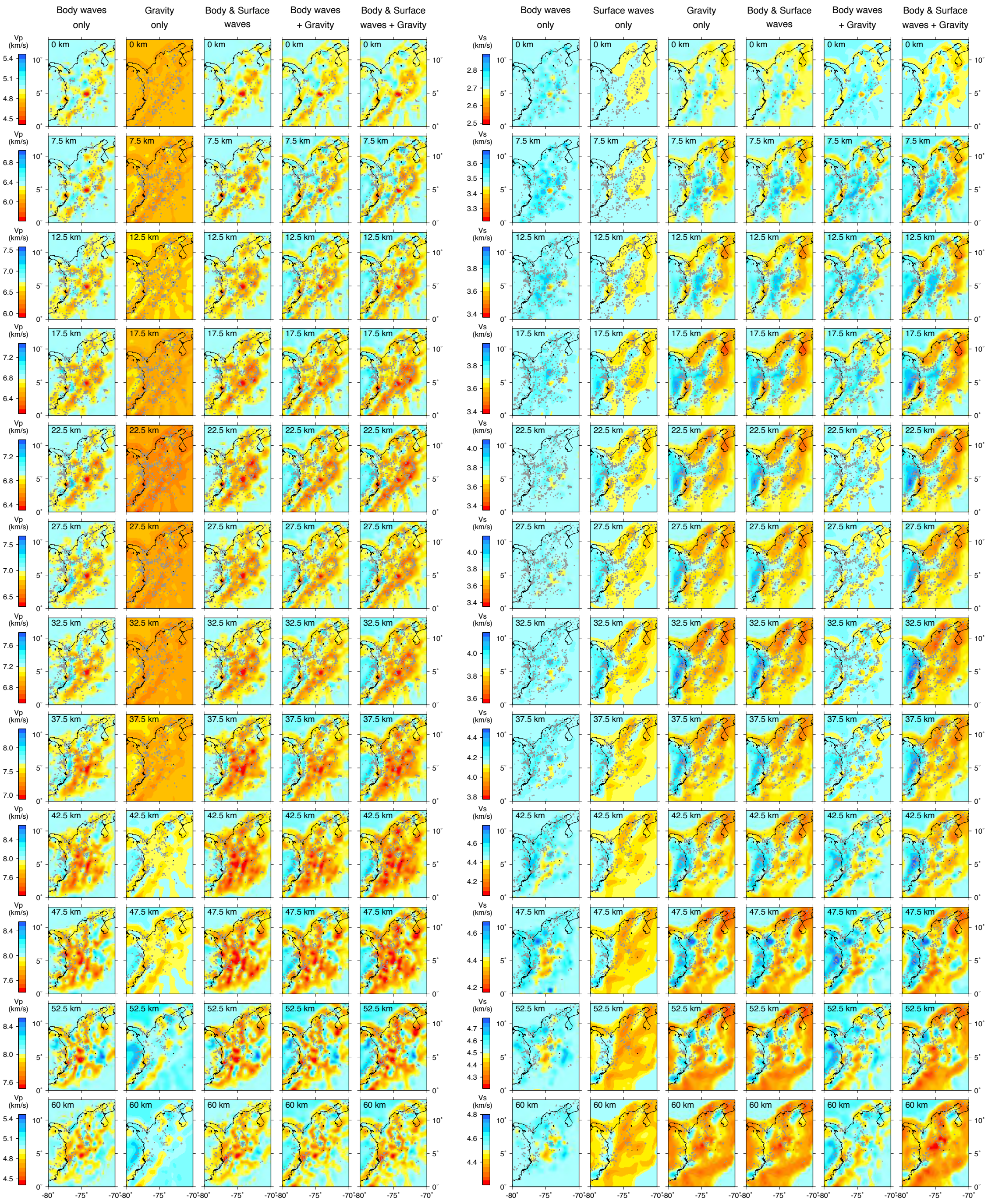
Body waves only
Gravity only
Body & Surface waves
Body waves + Gravity
Body & Surface waves + Gravity
Body waves only
Surface waves only
Gravity only
Body & Surface waves
Body waves + Gravity
Body & Surface waves + Gravity
Vp (km/s)
Vs (km/s)
0 km
7.5 km
12.5 km
17.5 km
22.5 km
27.5 km
32.5 km
37.5 km
42.5 km
47.5 km
52.5 km
60 km
5.4
5.1
4.8
4.5
6.8
6.4
6.0
7.5
7.0
6.5
6.0
7.2
6.8
6.4
7.2
6.8
6.4
7.5
7.0
6.5
7.6
7.2
6.8
8.0
7.5
7.0
8.4
8.0
7.6
8.4
8.0
7.6
8.4
8.0
7.6
5.4
5.1
4.8
4.5
2.8
2.7
2.6
2.5
3.6
3.5
3.4
3.3
3.8
3.6
3.4
3.8
3.6
3.4
4.0
3.8
3.6
3.4
4.0
3.8
3.6
3.4
4.0
3.8
3.6
4.4
4.2
4.0
3.8
4.6
4.4
4.2
4.6
4.4
4.2
4.7
4.6
4.5
4.4
4.3
4.8
4.6
4.4
10˚
5˚
0˚
-80˚
-75˚
-70˚

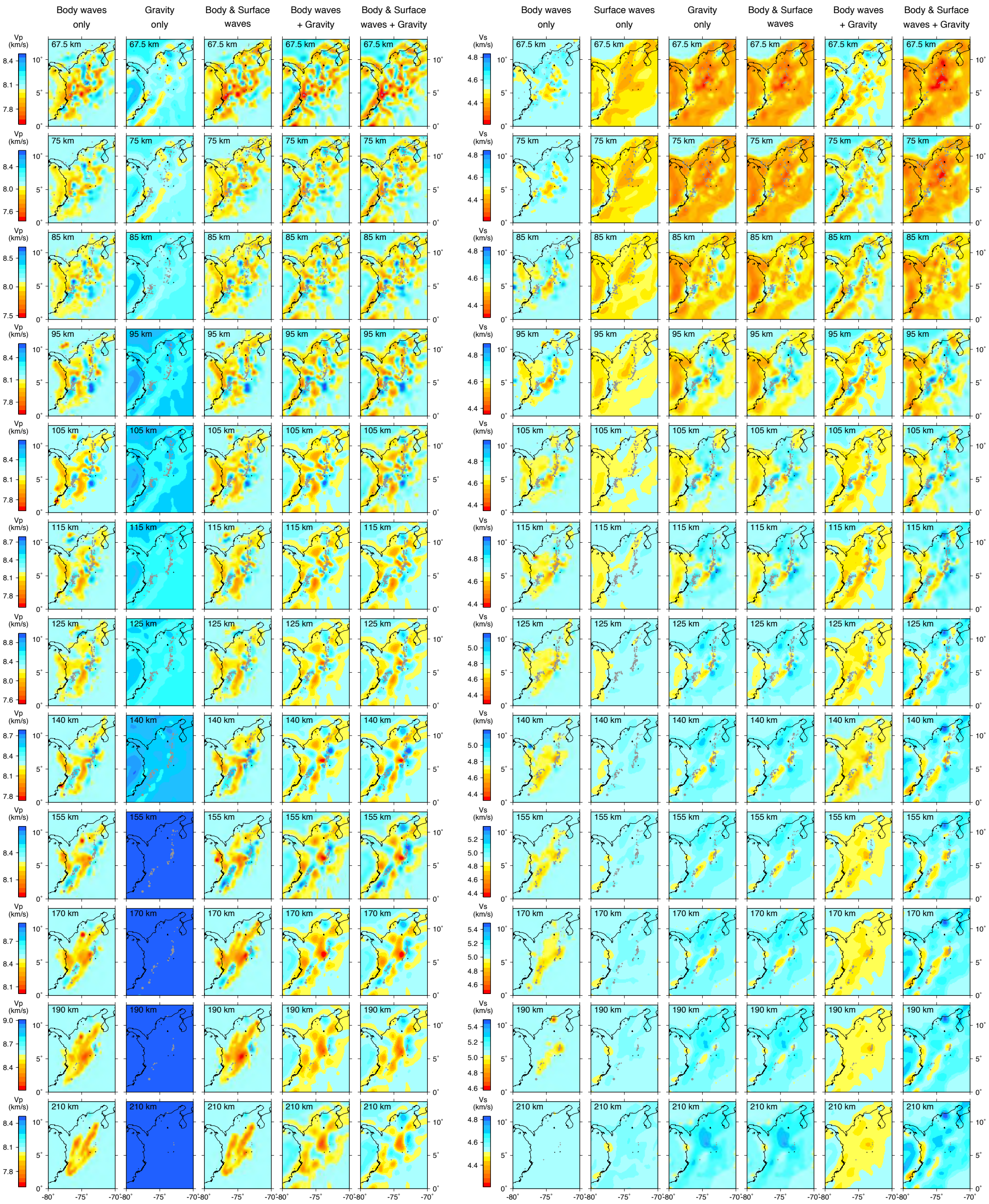

Supplemental Figure 3: Maps of velocity from inversions of different combinations of datasets, plotted at each node layer at or above 210 km depth. For inversions using two datasets, the same relative weights are used as in the full inversion, as discussed in Section 3.4. No Vp model is shown for the surface wave only inversion because Vp is not perturbed from the starting model.

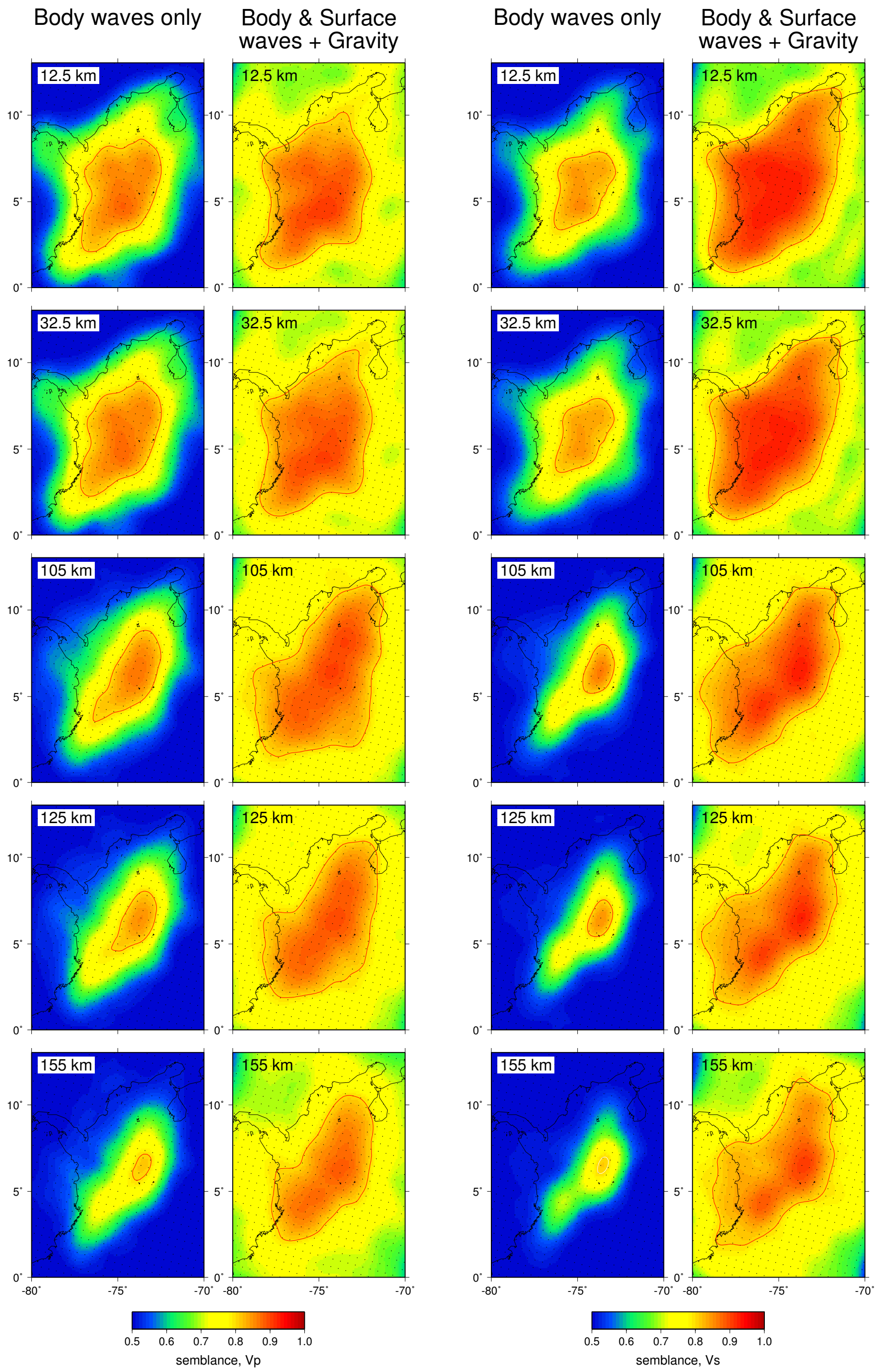

Supplemental Figure 4: Maps of average semblance resulting from inversions of 100 random input models. Regions with average semblance values above 0.8 (outlined in red) are considered the well-recovered portions of the model. Results for both body-wave-only inversions and full joint inversions are shown.

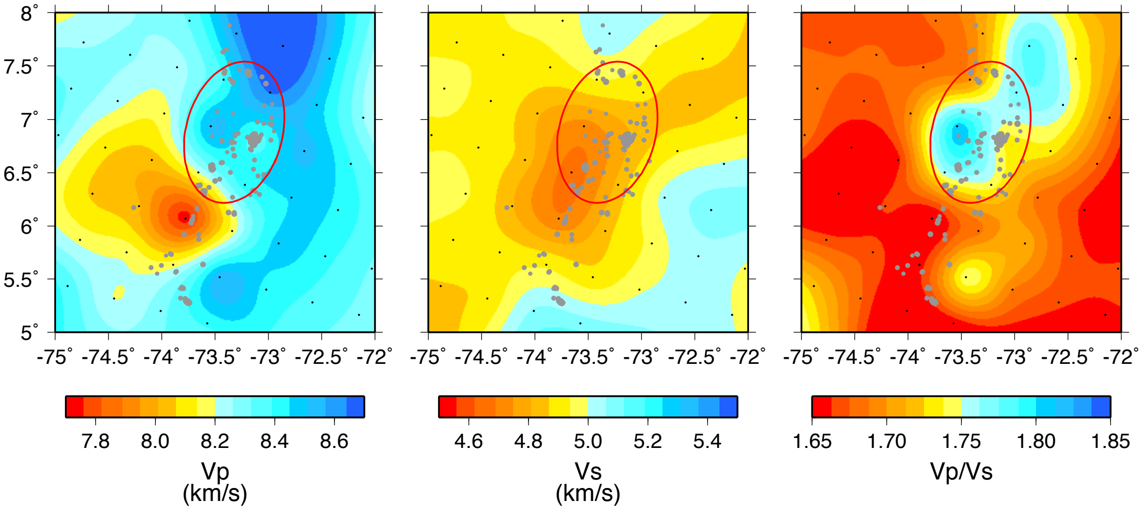

Supplemental Figure 5: Maps of Vp, Vs, and Vp/Vs, centered on the Bucaramanga nest, at 155 km depth. Nodes considered when calculating Vp/Vs surrounding the Bucaramanga nest (Section 5.1.2) are highlighted in red.

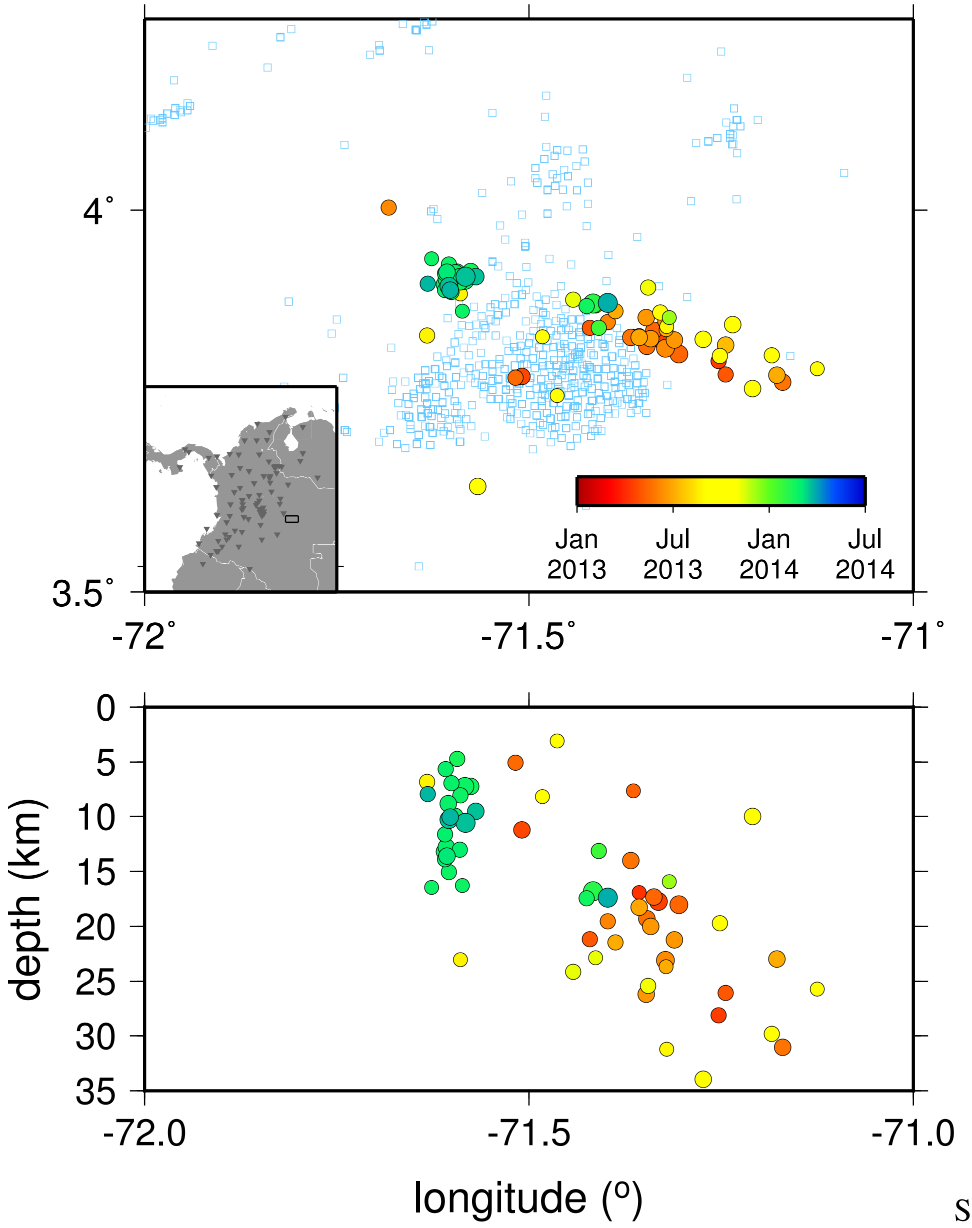

Supplemental

Figure 6: Map view and W-E cross section showing induced seismicity beginning April 2013, colored by time. Wells in the region are shown by light blue squares.